



ELSEVIER



Available online at www.sciencedirect.com

ScienceDirect

Comput. Methods Appl. Mech. Engrg. 358 (2020) 112622

Computer methods
in applied
mechanics and
engineering

www.elsevier.com/locate/cma

On Lagrangian mechanics and the implicit material point method for large deformation elasto-plasticity

William M. Coombs^{a,*}, Charles E. Augarde^a, Andrew J. Brennan^b, Michael J. Brown^b,
Tim J. Charlton^a, Jonathan A. Knappett^b, Yousef Ghaffari Motlagh^c, Lei Wang^a

^a *Department of Engineering, Durham University, UK*

^b *School of Science and Engineering, University of Dundee, UK*

^c *Department of Civil and Structural Engineering, University of Sheffield, UK*

Received 17 July 2018; received in revised form 3 September 2019; accepted 5 September 2019

Available online xxx

Abstract

The material point method is ideally suited to modelling problems involving large deformations where conventional mesh-based methods would struggle. However, total and updated Lagrangian approaches are unsuitable and non-ideal, respectively, in terms of formulating equilibrium for the method. This is due to the basis functions, and particularly the derivatives of the basis functions, of material point methods normally being defined on an unformed, and sometimes regular, background mesh. It is possible to map the basis function spatial derivatives using the deformation at a material point but this introduces additional algorithm complexity and computational expense. This paper presents a new Lagrangian statement of equilibrium which is ideal for material point methods as it satisfies equilibrium on the undeformed background mesh at the start of a load step. The formulation is implemented using a quasi-static implicit algorithm which includes the derivation of the consistent tangent to achieve optimum convergence of the global equilibrium iterations. The method is applied to a number of large deformation elasto-plastic problems, with a specific focus of the convergence of the method towards analytical solutions with the standard, generalised interpolation and CPDI2 material point methods. For the generalised interpolation method, different domain updating methods are investigated and it is shown that all of the current methods are degenerative under certain simple deformation fields. A new domain updating approach is proposed that overcomes these issues. The proposed material point method framework can be applied to all existing material point methods and adopted for implicit and explicit analysis, however its advantages are mainly associated with the former.

© 2019 The Authors. Published by Elsevier B.V. This is an open access article under the CC BY license (<http://creativecommons.org/licenses/by/4.0/>).

Keywords: Material point method; Lagrangian mechanics; Elasto-plasticity; Finite deformation mechanics; Generalised interpolation

1. Introduction

Numerical approaches based on Lagrangian mechanics, particularly using the finite element method, dominate the analysis of solid mechanics problems. However there are issues with mesh-based Lagrangian approaches for

* Corresponding author.

E-mail address: w.m.coombs@durham.ac.uk (W.M. Coombs).

problems involving very large deformation in that the discretisation used to analyse the physical problem becomes distorted leading to inaccurate results and, in extreme cases, eventual breakdown of the numerics due to element inversion. The material point method (MPM) is an alternative to pure Lagrangian approaches and is well suited to problems involving very large deformations. The method was developed in the 1990s by Sulsky and co-workers [1] as a solid mechanics extension to the FLuid Implicit Particle (FLIP) method [2] which itself was developed from the Particle-In-Cell (PIC) method [3]. In the material point method, equilibrium computations take place on a background grid but the calculations are based on information (mass, volume, stress, state variables, etc.) held at material points that are convected through the background grid as the material deforms. This allows computations to take place on an undistorted background mesh (structured or unstructured) whilst modelling problems involving very large deformations. One way to summarise the material point method is: *a finite element method where the integration points (material points) are allowed to move independently of the mesh.*

One of the most commonly cited drawbacks of the material point method is its inherent cell-crossing instability caused by the sudden transfer of mass, stiffness, internal force, etc. as a material point crosses between background elements. There have been several approaches proposed to mitigate this issue including the Generalised Interpolation Material Point (GIMP) method [4], the Convected Particle Domain Interpolation (CPDI) method [5], the second order Convected Particle Domain Interpolation (CPDI2) method [6,7] and Dual Domain Material Point (DDMP) methods [8–11]. Conceptually these methods are similar in that the discrete material point used in the standard material point method is replaced by a deformable material point domain which provides a gradual transition of information as a material point moves between background grid elements. An alternative is to adopt an additional level of smoothing, such as in the moving least squares modified material point method [12,13] or the weighted least squares approach of Wallstedt and Guilkey [14]. Another alternative is to use different basis functions which offer increased smoothness between elements, such as B-splines or cubic splines [15–18]. In this paper we examine the standard, generalised interpolation and CPDI2 material point methods, however the findings from this research can be applied to other material point methods with only modification of the basis functions. Three different material point methods are considered as, in the authors' experience, different material point variants are well suited to modelling different types of problems and some of the latest material point methods can become unstable under certain deformation fields (such as large distortion, shear and/or rotation), these points are explored in detail in Wang et al. [19].

The majority of material point papers implement the method using an explicit approach [20], however there are benefits of using an implicit approach [21–25] namely: (i) improved stability, (ii) error control and (iii) increased load step size. However, implicit approaches are more complex than explicit approaches in that they require the discrete equilibrium equations to be linearised with respect to the primary grid unknowns (typically incremental displacements). As the focus of this paper is on equilibrium formulations within the material point method, we adopt an implicit approach for quasi-static analysis as this allows precise error control when satisfying the governing equations.

Although the material point method is focused on solving large deformation problems, the precise application of finite deformation Lagrangian mechanics is a neglected area in the development of material point methods to date. In the authors' opinion this is due to a number of reasons: (i) the vast majority of current material point method codes are based on explicit time integration¹; (ii) it is assumed that standard finite element technology can be adopted without modification; and (iii) the majority of recently published material point method papers are focused on the application of the method rather than its fundamental development.²

Lagrangian mechanics for large deformation analysis is broadly split into two approaches; total and updated formulations which use material and spatial descriptions of motion, respectively. In particular they differ in the frame in which equilibrium is satisfied. In total Lagrangian approaches the equilibrium equations are formulated based on the reference, or original, frame whereas in updated Lagrangian formulations equilibrium is satisfied at the current, or deformed, state. Most material point approaches use an updated Lagrangian formulation as it is a more natural fit with the method. This is because, unlike conventional finite element methods, in the material point

¹ A consequence of adopting a forward-marching explicit scheme is that equilibrium is not checked at each load or time step and the calculations for the current step are based on information at the start of the step. It is only when equilibrium is satisfied at the end of the step, as in implicit approaches, that the issues discussed in this paper become apparent.

² This is particularly apparent from the focus of the papers at the first international conference on the material point method held in Delft in January 2017, [accessed 20/06/2018].

method information between the original and current background meshes (where equilibrium is actually satisfied) is lost by the fact that at the end of each load/time step the mesh is reset or replaced. Although possible, this makes mapping information, specifically spatial derivatives of the basis functions, back to the reference frame cumbersome for a total Lagrangian approach (this point is expanded upon later in the paper).

This paper first reviews the applicability of total and updated Lagrangian mechanics formulations for use with the material point method. The paper then proposes a new approach which formulates the statement of equilibrium in the *previously converged* frame. This previously converged Lagrangian formulation is well suited to material point methods as, unlike total/updated Lagrangian approaches, it allows all calculations to take place on an undeformed background mesh from the start of the load/time step. The approach allows the basis functions (and their spatial derivatives) to be calculated once per load step and used until equilibrium is achieved, reducing one of the significant costs in domain-based material point methods (GIMP, CPDI1, CPDI2, etc.). In addition to this, for the generalised interpolation material point method the basis functions are only defined in terms of regular background grids and the use of an updated Lagrangian approach requires the derivatives of these basis functions to be mapped into the current frame [21,26]. The paper also explores different domain updating procedures for the generalised interpolation material point method and shows that the existing approaches are inappropriate for some basic deformation fields. A new approach is proposed which overcomes the limitations of existing methods.

The formulations presented in this paper can be applied to both implicit and explicit approaches but it is with the former where the advantages of the formulation are apparent. This is because explicit approaches advance a simulation through forward prediction based on the *state* of the analysis at the start of the load (or time) step. In this case the updated Lagrangian and previously converged Lagrangian formulations are identical as the load step has yet to experience any deformation.

2. Large deformation mechanics

This paper is restricted to quasi-static finite deformation mechanics with isotropic elasto-plastic material behaviour with a multiplicative decomposition of the deformation gradient into elastic and plastic components combined with a linear relationship between elastic logarithmic strains and Kirchhoff stresses. For the sake of brevity details of the large deformation framework are not given here, instead the interested reader is referred to [19,21,26] for more information.

3. Updated Lagrangian formulation

This section details the quasi-static implicit finite deformation elasto-plastic material point method based on an updated Lagrangian formulation³ defined by the following weak statement of equilibrium

$$\int_{\varphi_t(\Omega)} \left(\sigma_{ij} (\nabla_x \eta)_{ij} - b_i \eta_i \right) dv - \int_{\varphi_t(\partial\Omega)} \left(t_i \eta_i \right) ds = 0. \tag{1}$$

φ_t is the motion of the material body with domain, Ω , which is subjected to tractions, t_i , on the boundary of the domain (with surface, s), $\partial\Omega$, and body forces, b_i , acting over the volume, v of the domain, which lead to a Cauchy stress field, σ_{ij} , through the body. The weak form is derived in the current frame assuming a field of admissible virtual displacements, η_i .

3.1. Discrete material point formulation

The Galerkin form of the weak statement of equilibrium over each background grid element, E , can be obtained from (1) as

$$\int_{\varphi_t(E)} [\nabla_x S_{vp}]^T \{\sigma\} dv - \int_{\varphi_t(E)} [S_{vp}]^T \{b\} dv - \int_{\varphi_t(\partial E)} [S_{vp}]^T \{t\} ds = \{0\}, \tag{2}$$

where $[\nabla_x S_{vp}]$ is the tensorial form of the strain–displacement matrix containing derivatives of the shape functions with respect to the updated coordinates and $\{\sigma\}$ is the nine-component vector form of σ_{ij} . The first term in (2) is

³ This is the same formulation as implemented in the generalised interpolation approach of Charlton et al. [21] but has been included here for completeness and so that particular aspects of the formulation can be emphasised.

the internal force within an element and the combination of the second (body forces) and third (tractions) terms is the external force vector. Eq. (2) is non-linear in terms of the unknown nodal displacements and can be efficiently solved using the standard implicit Newton–Raphson (N–R) procedure (see Section 6.3). This requires (2) to be linearised with respect to the nodal displacements to arrive at the stiffness of each element in the background mesh

$$[k^E] = \int_{\varphi_r(E)} [\nabla_x S_{vp}]^T [a][\nabla_x S_{vp}] dv, \tag{3}$$

where $[a]$ is the matrix form of $a_{ijkl} = (\partial\sigma_{ij}/\partial F_{km})F_{lm}$, which is the spatial consistent tangent modulus for a point within the element which is detailed in Appendix A.1.

In material point methods the physical domain is discretised by a number of material points. These points are used to numerically approximate the stiffness (3) of the elements in the background mesh, essentially replacing the conventional Gauss points (or other integration method). The key difference between material point and finite element methods is that these integration points move relative to the background mesh rather than being directly coupled to the positions of the background grid nodes. The stiffness contribution of a single material point to the background mesh is

$$[k_p] = [\nabla_x S_{vp}]^T [a][\nabla_x S_{vp}] V_p, \tag{4}$$

where V_p is the volume associated with the material point in the spatial (updated) frame

$$V_p = \det(\Delta F_{ij}) V_p^n = \det(F_{ij}) V_p^0, \tag{5}$$

where V_p^n and V_p^0 are the volume associated with the material point in the previously converged state and the initial configuration, respectively. The internal force contribution of a single material point to the background mesh is

$$\{f^p\} = [\nabla_x S_{vp}]^T \{\sigma\} V_p. \tag{6}$$

Following the work of Charlton et al. [21], and as adopted by Coombs et al. [26], the increment in the deformation gradient is obtained from

$$\Delta F_{ij} = \delta_{ij} + \frac{\partial \Delta u_i}{\partial \tilde{X}_j} = \delta_{ij} + \sum_{v=1}^n (\Delta u_v)_i \frac{\partial (S_{vp})}{\partial \tilde{X}_j}, \tag{7}$$

where Δu_i is the displacement increment within the current load step, \tilde{X}_j are the coordinates at the start of the load step and n is the number of nodes that influence the material point. This allows the increment in the deformation gradient to be obtained from derivatives of the basis functions based on the coordinates of the nodes at the start of the load step. This is essential as in material point methods there is no concept of the current (deformed) nodal coordinates as information is lost between incremental steps. Also, the basis functions for material point methods are typically only defined on a regular background grid. The spatial derivatives of the basis functions can subsequently be calculated using the method proposed in Charlton et al. [21], that is

$$\frac{\partial (S_{vp})}{\partial x_j} = \frac{\partial (S_{vp})}{\partial \tilde{X}_i} \frac{\partial \tilde{X}_i}{\partial x_j} = \frac{\partial (S_{vp})}{\partial \tilde{X}_i} (\Delta F_{ij})^{-1}. \tag{8}$$

It is essential that the spatial derivatives are used in the strain–displacement matrix, $[\nabla_x S_{vp}]$, to both ensure the correct order of convergence in the N–R process and convergence towards the correct solution based on the internal force contribution, (6), of each material point [21,26].

For the standard material point method an alternative to mapping the derivatives of the basis functions into the spatial frame using (8) is to calculate the spatial derivatives of the basis functions using the standard finite element Jacobian mapping based on the deformed nodal positions. However, this is only possible for certain material point methods as some domain-based material point formulations, such as the generalised interpolation material point method, rely on a regular background grid.

It is not necessary to map the basis functions between the start of the load step and the current configuration because it is assumed that, during a load step, the displacement of a material point, $(\Delta u_p)_i$, is linked to the nodal displacements through the basis functions, S_{vp} , that is

$$(\Delta u_p)_i = \sum_{v=1}^n S_{vp} (\Delta u_v)_i, \tag{9}$$

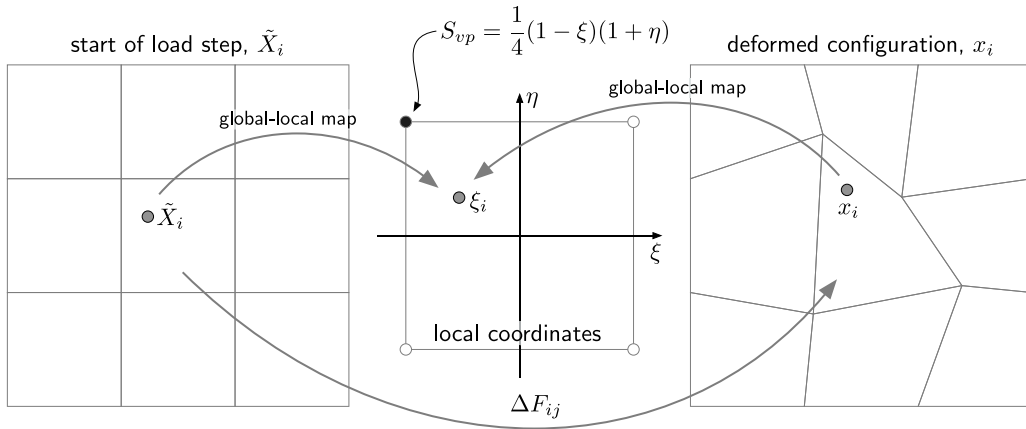


Fig. 1. Global–local map for the deformed frame and the configuration at the start of the load step.

where n is the number of nodes that influence the material point and $(\Delta u_v)_i$ are the displacement of the nodes over the current load step. Therefore the basis functions evaluated at the start or the end of the load step are identical, as shown in Fig. 1. The figure shows a single material point on a background mesh at the start and end (deformed configuration) of the load step. It also shows the local coordinates, ξ_i , of the material point’s parent element and gives the basis function for a single node (dark-grey shaded). The local position of the material point is the same throughout the load step and therefore the basis functions are also constant, whereas the spatial derivatives of the basis functions are dependent on the deformation over the load step.

4. Total Lagrangian formulation

This section details the quasi-static implicit finite deformation elasto-plastic material point method based on a total Lagrangian formulation defined by the following weak statement of equilibrium

$$\int_{\Omega} \left(P_{ij}(\nabla_X \eta)_{ij} - b_i \eta_i \right) dv - \int_{\partial\Omega} \left(t_i \eta_i \right) ds = 0, \tag{10}$$

where the reference domain, Ω , is subjected to tractions, t_i , on the boundary of the domain (with surface, s), $\partial\Omega$, and body forces, b_i , acting over the volume, v of the domain, which lead to a first Piola Kirchhoff stress field, $P_{ij} = J \sigma_{ik} F_{jk}^{-1}$, throughout the body. The weak form is derived in the reference (or material) frame assuming a field of admissible virtual displacements, η_i , and the derivatives of these virtual displacements in the first term in (10) are taken with respect to the original material coordinates, X_i .

4.1. Discrete material point formulation

The Galerkin form of the weak statement of equilibrium over each background grid element, E , can be obtained from (10) as

$$\int_E [\nabla_X S_{vp}]^T \{P\} dv - \int_E [S_{vp}]^T \{b\} dv - \int_{\partial E} [S_{vp}]^T \{t\} ds = \{0\}, \tag{11}$$

where $[\nabla_X S_{vp}]$ is the tensorial form of the strain–displacement matrix and contains the derivatives of the basis functions, $[S_{vp}]$, with respect to the original coordinates. The first term in (11) is the internal force within an element and the combination of the second (body forces) and third (tractions) terms is the external force vector.

In material point methods, at the end of each load (or time) step the background mesh is reset or replaced. This causes issues when trying to adopt a total Lagrangian formulation as information is lost regarding the deformation of the background mesh between load steps. For example, the strain–displacement matrix requires the derivatives of the basis functions with respect to the original coordinates, but there is no guarantee that a material point is in

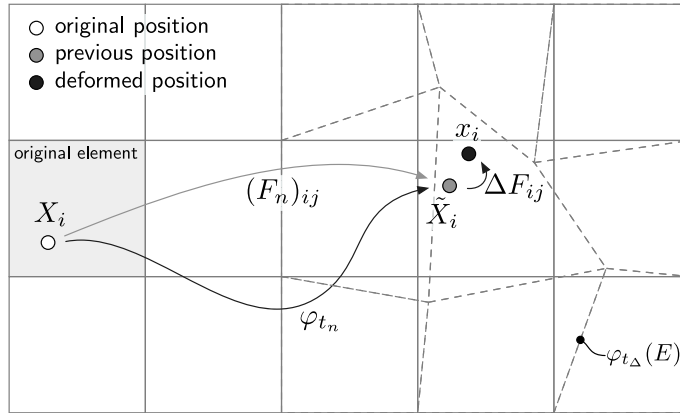


Fig. 2. Motion and deformation of a material point from the reference frame to the current configuration, where $\varphi_{t\Delta}$ denotes the motion over the current load step and the original and deformed meshes are shown by the solid and dashed grey lines, respectively.

the same element as at the start of the analysis. It is possible to map the derivatives of the basis functions back to the reference frame using

$$\frac{\partial S_{vp}}{\partial X_i} = \frac{\partial S_{vp}}{\partial \tilde{X}_j} \frac{\partial \tilde{X}_j}{\partial X_i} = \frac{\partial S_{vp}}{\partial \tilde{X}_j} (F_n)_{ji} \quad \text{or} \quad \frac{\partial S_{vp}}{\partial X_i} = \frac{\partial S_{vp}}{\partial x_j} \frac{\partial x_j}{\partial X_i} = \frac{\partial S_{vp}}{\partial x_j} F_{ji}, \tag{12}$$

but these derivatives would be associated with the material point’s current element. There are also issues associated with determining the external force vector in the reference frame due to the material points moving between elements. Some of these issues are highlighted by Fig. 2 which shows the motion and deformation of a material point from the reference frame to the current configuration. The material point is initially located in the grey-shaded element and over a number of load steps it has moved to \tilde{X}_i and in the current load step has deformed to x_i with an associated increment in the deformation gradient. The deformed mesh in the current load step is shown by the grey dashed line and the original mesh by the grey solid lines. Consider the calculation of the nodal body forces associated with the material point as it convects through the background mesh. After the initial load step the material point’s local position within an element, and its associated basis functions, will change. Therefore, if we attempted to satisfy equilibrium in the reference frame using (11) we would have to map the basis functions back to the original coordinates. In the authors’ opinion this is not practical as it would require mesh deformation throughout the analysis to be stored, destroying one of the key advantages of the material point method. Therefore we feel that it is inappropriate to combine a total Lagrangian formulation with the material point method.

5. Previously converged formulation

This section provides a new approach for satisfying equilibrium in the material point method.⁴ The updated Lagrangian weak statement of equilibrium (1) can be recast within a *previously converged* formulation where equilibrium is satisfied at the starting point of a load step (or the previously converged state). The statement of equilibrium becomes

$$\int_{\varphi_{t_n}(\Omega)} \left(\tilde{P}_{ij} (\nabla_{\tilde{x}} \eta)_{ij} - b_i \eta_i \right) dv - \int_{\varphi_{t_n}(\partial\Omega)} (t_i \eta_i) ds = 0, \tag{13}$$

where φ_{t_n} is the motion of the material body evaluated at the previously converged (or for the first load step, the initial) state and \tilde{P}_{ij} is the Cauchy stress pulled back to the previously converged state, \tilde{X}_i , that is

$$\tilde{P}_{ij} = \Delta J \sigma_{im} (\Delta F^{-1})_{jm}, \tag{14}$$

⁴ The approach can equally be applied to other continuum mechanics methods, for example those based on finite elements, but it is particularly suited to the material point method due to the way that the basis functions are calculated.

where σ_{ij} is the Cauchy stress, ΔF_{ij} is the deformation gradient increment over the load step and $\Delta J = \det(\Delta F_{ij})$ is the volume ratio between the current and previously converged state. (14) can be expressed in terms of the Kirchhoff stress, τ_{ij} as

$$\tilde{P}_{ij} = \frac{\Delta J}{J} \tau_{im} (\Delta F^{-1})_{jm}, \quad (15)$$

where $J = \det(F_{ij})$. Using the fact that the current deformation gradient can be obtained using

$$F_{ij} = \Delta F_{im} (F_n)_{mj}, \quad (16)$$

where $(F_n)_{ij}$ is the deformation gradient from the previously converged state, and

$$J = \det(F_{ij}) = \det(\Delta F_{im} (F_n)_{mj}) = \Delta J J_n, \quad (17)$$

(15) becomes

$$\tilde{P}_{ij} = \frac{1}{J_n} \tau_{im} (\Delta F^{-1})_{jm}. \quad (18)$$

This particular form is useful when linearising \tilde{P}_{ij} with respect to the deformation gradient increment over a load step as J_n is constant over the load step. The next section presents the discrete material point approach for this previously converged formulation.

5.1. Discrete material point formulation

The Galerkin form of the weak statement of equilibrium for the approach described above over each background grid element, E , can be obtained from (13) as

$$\{f^R\} = \int_{\varphi_n(E)} [\nabla_{\tilde{x}} S_{vp}]^T \{\tilde{P}\} dv - \int_{\varphi_n(E)} [S_{vp}]^T \{b\} dv - \int_{\varphi_n(\partial E)} [S_{vp}]^T \{t\} ds = \{0\}, \quad (19)$$

where $[\nabla_{\tilde{x}} S_{vp}]$ is the tensorial form of the strain–displacement matrix containing derivatives of the basis functions with respect to the nodal coordinates at the start of the load step. As with (2), (19) is non-linear in terms of the unknown nodal displacements and can be solved in the same way, the only difference being where equilibrium is satisfied. The N–R solution procedure is detailed in Section 6.3.

The element stiffness matrix can be obtained by linearising the discrete statement of equilibrium with respect to the unknown nodal displacements to give

$$[\tilde{k}^E] = \int_{\varphi_n(E)} [\nabla_{\tilde{x}} S_{vp}]^T [\tilde{A}] [\nabla_{\tilde{x}} S_{vp}] dv, \quad (20)$$

where $\tilde{A}_{ijkl} = \partial \tilde{P}_{ij} / \partial \Delta F_{kl}$ is the previously converged consistent tangent modulus and its derivation is detailed in Appendix A.2. The stiffness contribution of a single material point to the background mesh is

$$[\tilde{k}_p] = [\nabla_{\tilde{x}} S_{vp}]^T [\tilde{A}] [\nabla_{\tilde{x}} S_{vp}] V_p^n, \quad (21)$$

where V_p^n is the volume associated with the material point at the end of the previously converged (or the start of the current) load step

$$V_p^n = \det((F_n)_{ij}) V_p^0. \quad (22)$$

The internal force contribution of a single material point to the background mesh is

$$\{\tilde{f}^p\} = [\nabla_{\tilde{x}} S_{vp}]^T \{\tilde{P}\} V_p^n. \quad (23)$$

The advantage of the proposed formulation is that it does not require the derivatives of the basis functions to be mapped into the spatial (8) or material (12) frames as in the updated and total Lagrangian formulations, respectively. Therefore all equilibrium calculations truly take place on the background mesh at the start of the load step before the material points are convected through the mesh once equilibrium has been obtained.

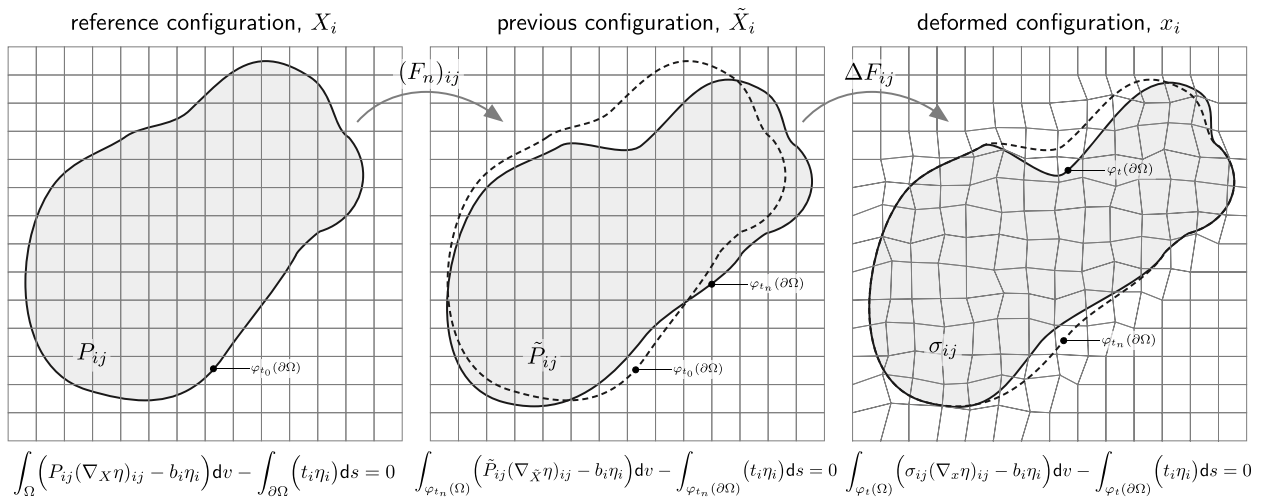


Fig. 3. Original, previous and deformed configurations with statements of equilibrium in each frame. The physical domain is shown by the grey-shaded body and while the shape of the domain from the preceding frame is shown by the dashed line.

Table 1

Comparison of key quantities required for total, updated and previously converged Lagrangian approaches.

Lagrangian formulation	Total	Updated	Previous
Coordinates	X_i	x_i	\tilde{X}_i
Equilibrium stress measure	P_{ij}	σ_{ij}	\tilde{P}_{ij}
Consistent volume	V_p^0	V_p	V_p^n
Basis derivatives	$\nabla_X S_{vp}$	$\nabla_x S_{vp}$	$\nabla_{\tilde{X}} S_{vp}$
Derivative map (from previous)	$(F_n)_{ij}^{-1}$	ΔF_{ij}^{-1}	–
Consistent tangent	$\partial P_{ij} / \partial F_{kl}$	$(\partial \sigma_{ij} / \partial F_{km}) F_{lm}$	$\partial \tilde{P}_{ij} / \partial \Delta F_{kl}$

The total, updated and previously converged formulations are compared and contrasted in Fig. 3 and Table 1. Fig. 3 shows a deforming domain, the grey-shaded body, in the reference, previous and deformed configurations along with the mesh associated with these frames. The reference, X_i , and previous, \tilde{X}_i , configurations are linked by the deformation gradient at the previously converged state, $(F_n)_{ij}$, and the stress measures that are used to satisfy equilibrium in these frames are P_{ij} and \tilde{P}_{ij} , respectively. The previous and current, x_i configurations are linked by the deformation gradient increment over the load step, ΔF_{ij} , and the Cauchy stress, σ_{ij} , is used to satisfy the equilibrium equations in this deformed frame. The dashed shapes shows the domain from the preceding frame, for example in the previous configuration the dashed line shows the domain in the reference configuration and for the deformed configuration the dashed line shows the previous configuration. In the reference and previous configurations calculations take place on undeformed background meshes whereas in the updated Lagrangian approach equilibrium is satisfied on the current, deformed mesh. Table 1 highlights key quantities associated with the different formulations.

The proposed *previously converged* formulation shares some similarities with incremental non-linear elasticity where small deformations are superimposed on a given equilibrium state, see for example Bigoni [27]. However, in that work it is assumed that the deformation between the current and previous state is small, leading to a linear set of equations, whereas no such assumption is made here and we allow for finite (and non-linear) deformations within each step. There are also similarities with co-rotational formulations⁵ that decompose the total deformation into stretch and rotation and map the equilibrium coordinates according to the material rotation. However, the

⁵ See Belytschko et al. [28], amongst others, for a textbook account of these co-rotational methods.

formulation proposed in this paper uses the entire deformation (stretch and rotation) when defining the equilibrium state based on the deformation at the end of the previous load step.

6. Implementation aspects

This section presents key information regarding the implementation of the finite deformation formulations detailed in the previous sections. This includes the basis functions for the implemented material point methods, boundary conditions and material point position/domain updating.

6.1. Basis functions

The basis functions for the standard material point method are the same as conventional finite element analysis and the basis functions for the other methods are available from: [4,21] for the generalised interpolation method and [6] for CPDI2 with quadrilateral domains.⁶

6.2. Boundary conditions

In this paper we ignore the external tractions as their general implementation within material point methods has yet to be fully clarified due to the uncertain definition of the boundary of the physical domain. It is noted that in domain-based material point methods (GIMP, CPDI1, CPDI2) it is possible to specify surface tractions on the outer boundaries of the material point domains and Bing et al. [29] and Remmerswaal [30] have gone some way to addressing this issue for the standard material point method.

In this work, Dirichlet boundary conditions are imposed directly on the background mesh in the same way as the standard finite element method. This places some restrictions on the form of the boundary conditions that can be applied to the material point method, which have been overcome by the recent work of Cortis et al. [31], Bing [32] and Bing et al. [29]. However, the focus on this paper is the use of different continuum mechanics formulations with the material point method and all of the problems analysed in Section 7 can be modelled by imposing the Dirichlet boundary conditions on the background grid.

The body force in (2) or (19) is approximated using

$$\{f_b\} = [S_{vp}]^T \{b\} V_p^n, \quad (24)$$

where $\{b\}$ is the body force associated with the material point. Point forces, if required, are held and convected with the material points. They are mapped to the background grid using

$$\{f_P\} = [S_{vp}]^T \{f_p\}, \quad (25)$$

where $\{f_p\}$ is the point force associated with the material point and $\{f_P\}$ are the equivalent nodal values.

6.3. Non-linear solution procedure

The nodal displacements within a load step, $\{\Delta d\}$, can be obtained by iteratively updating the nodal displacements until (2) or (19), for the updated and previous Lagrangian formulations respectively, are satisfied within a given tolerance using

$$\{\delta d_k\} = [K]^{-1} \{f_{k-1}^R\}, \quad (26)$$

where k is the current iteration within the load step, $[K]$ is the global stiffness matrix and $\{\delta d_k\}$ is the iterative increment in the displacements from that iteration. The global stiffness matrix is obtained through assembling the individual material point contributions, for example for the previously converged formulation

$$[K] = \underset{V_p}{A} [\tilde{k}_p], \quad (27)$$

⁶ Note that the basis functions were incorrect in the original CPDI2 paper [6], the correct equation can be obtained from <https://csmbranon.net/tag/mpm/> [accessed 02/07/2019].

where \mathbf{A} is the standard assembly operator acting over all of the material points in the problem and $[\tilde{k}_p]$ is given by (21). $\{f_{k-1}^R\}$ is the residual out of balance force vector associated with the previous displacement value; the difference between the internal forces due to the stresses within the material and the applied boundary conditions, as given by (19) for the previously converged formulation. The global residual vector is assembled through

$$\{f_k^R\} = \mathbf{A}_{\forall p} \left([\nabla_{\tilde{x}} S_{vp}]^T \{\tilde{P}_k\} V_p^n \right) - \{f^{\text{ext}}\}, \tag{28}$$

where the first term is the internal force vector and the external force vector, $\{f^{\text{ext}}\}$, which is constant over the load step, is given by

$$\{f^{\text{ext}}\} = \mathbf{A}_{\forall p} \left([S_{vp}]^T \{b\} V_p^n + [S_{vp}]^T \{f_p\} \right) + \int_{\varphi_n(\partial E)} [S_{vp}]^T \{t\} ds. \tag{29}$$

The current displacement in a load step can be obtained by summing the iterative increments within the load step, that is

$$\{\Delta d_k\} = \sum_{n=1}^k \{\delta d_n\}, \tag{30}$$

where it is assumed that $\{\delta d_0\} = \{0\}$.

6.4. Position and domain updating

At the end of each load step the material point positions, volumes and (if appropriate) domain half-lengths, l_p , should be updated. The updated positions of the material points at the end of the load step are given by

$$(x_p)_i = (\tilde{X}_p)_i + \underbrace{\sum_{v=1}^n (S_{vp})(\Delta u_i)_v}_{(\Delta u_p)_i}, \tag{31}$$

where $(\Delta u_p)_i$ is the displacement of the material point over the load step.

In the case of the standard material point method the volume at each material point is simply updated from the original volume using the determinant of the deformation gradient, (5). In other methods that explicitly define a finite sized domain for each material point the process of domain updating is more complex. For generalised interpolation material point methods, one approach is to apply uniform expansion/contraction of domains according to the volume change at the material point using

$$l_i^p = l_i^{p0} \left(\det(F_{jk}) \right)^{1/n_D}, \tag{32}$$

where n_D is the physical dimensionality of the analysed problem. A commonly adopted approach is to update the domain sizes according to the normal components of the deformation gradient through

$$l_i^p = l_i^{p0} F_{ii} \quad (\text{no implied sum on } i), \tag{33}$$

where F_{ii} denotes one of the leading diagonal components of F_{ij} . An alternative domain updating method, proposed by Charlton et al. [21], is to map the domain sizes according to the normal components of the material stretch tensor, that is

$$l_i^p = l_i^{p0} U_{ii} \quad (\text{no implied sum on } i). \tag{34}$$

The suitability of these domain updating methods for different deformation modes is summarised in Table 2, which shows that both not updating the material point domains and updating them according to (32) are not suitable choices when analysing problems involving simple stretch as they fail to correctly account for changes in the physical size of the global domain in the stretched/compressed direction. The only exception to this is when modelling problems involving hydrostatic compression/expansion where (32) is a suitable choice due to the imposed uniform volume change. (33) and (34) are suitable for these types of problems, however they have issues under pure rotation and simple shear, respectively. These issues are demonstrated in Fig. 4. Fig. 4 (a) shows the case of

Table 2
Suitability of generalised interpolation domain updating methods with deformation modes.

Deformation mode	Domain updating method				
	No update	$\det(F_{ij})$, (32)	F_{ii} , (33)	U_{ii} , (34)	(37)
Simple stretch	× ^a	× ^b	✓	✓	✓
Hydrostatic comp./exten.	× ^a	✓	✓	✓	✓
Simple shear	✓	✓	✓	× ^c	✓
Pure rotation	✓	✓	× ^d	✓	✓

^aNon-zero volume change of the deformation mode not accounted for by the domain update.

^bArtificial orthogonal contraction/expansion of domains.

^cDomain volumes change under isochoric deformation.

^dVanishing material point domains with increasing rotation.

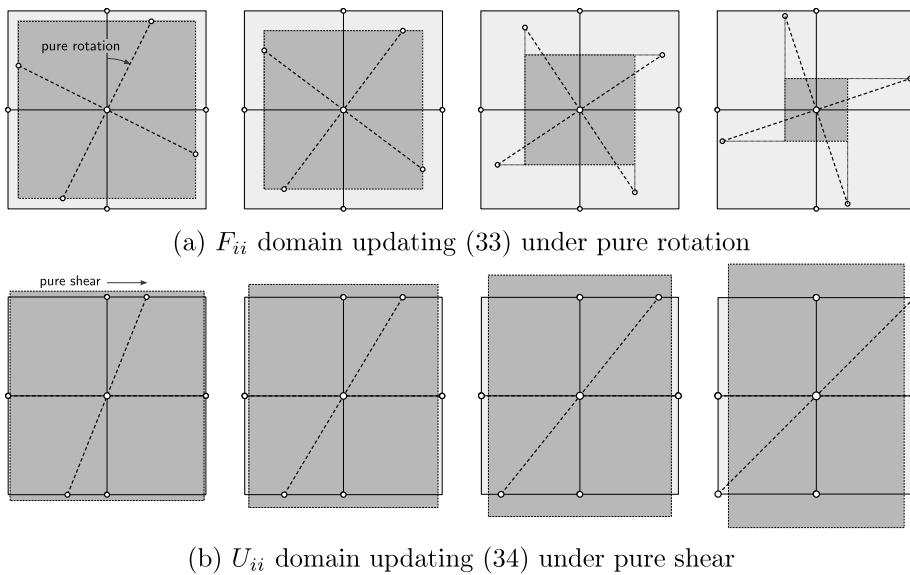


Fig. 4. Domain updating procedures under different deformation modes, where the light and dark grey shaded regions are the original and updated domains, respectively.

pure rotation where the domain is updated according to (33), where the light and dark grey shaded regions are the original and updated domains, respectively. The mid lines of the domain are identified by the solid black lines with the black-shaded circles and the deformed location of these lines are shown by the black dashed lines with the white-shaded circles. Under continued rotational deformation the material point’s domain shrinks but the physical volume of the particle should remain constant due to the isochoric nature of the deformation field. Fig. 4 (b) shows the case of pure shear where the domain is updated according to (34). In this case the domain expands in the y-direction whilst shrinking in the x-direction and the overall volume of the domain increases however, as in the case of pure rotation, the physical volume of the particle should remain constant due to the isochoric nature of the deformation field.

Here we propose a new domain updating method which is inspired by CPDI2 approaches in that the individual corners of a particle’s domain are updated according to the nodal deformation but, in order to maintain a rectangular domain, the midpoints of the updated limits of the domain are used to define the new l_i^p . The proposed procedure is shown in Fig. 5 (a) for a single generalised interpolation material point domain. The original domain is shown by the grey-shaded region and the original and the deformed corners of the domain identified by the white and

grey-filled circles, respectively. The corners of the domain are updated according to the basis functions associated with the background grid, that is

$$x_i^c = \tilde{X}_i^c + \sum_{v=1}^n S_{vp}(\Delta u_i)_v, \quad (35)$$

where \tilde{X}_i^c is the corner's position at the start of the load step. Once the updated positions of the domain corners have been determined, the midpoints of the edges can then be used to determine the new domain lengths through

$$l_i^{pm} = \frac{1}{2} \left(\max(x_i^m) - \min(x_i^m) \right) \quad (36)$$

where x_i^m are the updated locations of the domain edge midpoints. An alternative is to directly map the midpoints using the nodal deformations, as shown in Fig. 5 (b). The final part of the updating procedure is to ensure that the domain updating is consistent with the change in volume at the material point. This is achieved using

$$l_i^p = l_i^{pm} \left(\frac{\det(F_{kl}) \prod_{j=1}^{n_D} l_j^{p_0}}{\prod_{j=1}^{n_D} l_j^{pm}} \right)^{1/n_D} \quad (37)$$

which uniformly scales the size of the domain about the material point's location and accounts for any spurious changes in volume caused by pure rotational deformation.

Note that it is possible to apply a similar correction to the (33) domain updating method to ensure that the correct volume is maintained at the material point, such as

$$l_i^p = l_i^{p_0} F_{ii} \left(\frac{\det(F_{kl})}{\prod_{j=1}^{n_D} F_{jj}} \right)^{1/n_D} \quad (\text{no implied sum on } i). \quad (38)$$

However, there is still an issue with this approach when components of F_{ii} are equal to zero, such as the case of 90° rotation. An incremental form of (38), such as

$$l_i^p = l_i^{p_n} \Delta F_{ii} \left(\frac{\det(\Delta F_{kl})}{\prod_{j=1}^{n_D} \Delta F_{jj}} \right)^{1/n_D} \quad (\text{no implied sum on } i), \quad (39)$$

where $l_i^{p_n}$ is the domain length from the previously converged state, partially overcomes this issue, provided that excessive rotations are not experienced within a single load step. (32), (33) and (34) can also be cast in an incremental setting, if appropriate or convenient. Although the focus of the numerical examples presented in this paper is on two-dimensional analysis, it is straightforward to extend all of the above approaches to three dimensions and the above equations allow for this.

6.5. Computational procedure

This paper has described two approaches (updated Lagrangian and previous Lagrangian) to solve quasi-static large deformation elasto-plastic problems using implicit formulations of the standard, generalised interpolation and CPDI2 material point methods. Details of the computational procedure can be found in Coombs et al. [26].

7. Numerical examples

All of the results in this section use the *previously converged* formulation presented in Section 5. Adopting the updated Lagrangian formulation, as expected, gives identical results but is computationally less efficient due to the mapping of the basis derivatives between the previously converged state, where they are defined, and the current deformed state. Based on studies conducted by the authors, the computational saving of adopting the *previously converged* formulation is approximately 5% for two-dimensional analysis.

In all cases the global tolerance on the normalised out of balance force in the N-R process was set at 1×10^{-9} , where the normalised out of balance force was defined as

$$\bar{f}^R = \frac{\|\{f^R\}\|}{\|\{f^{\text{ext}}\} + \{f^{\text{react}}\}\|}. \quad (40)$$

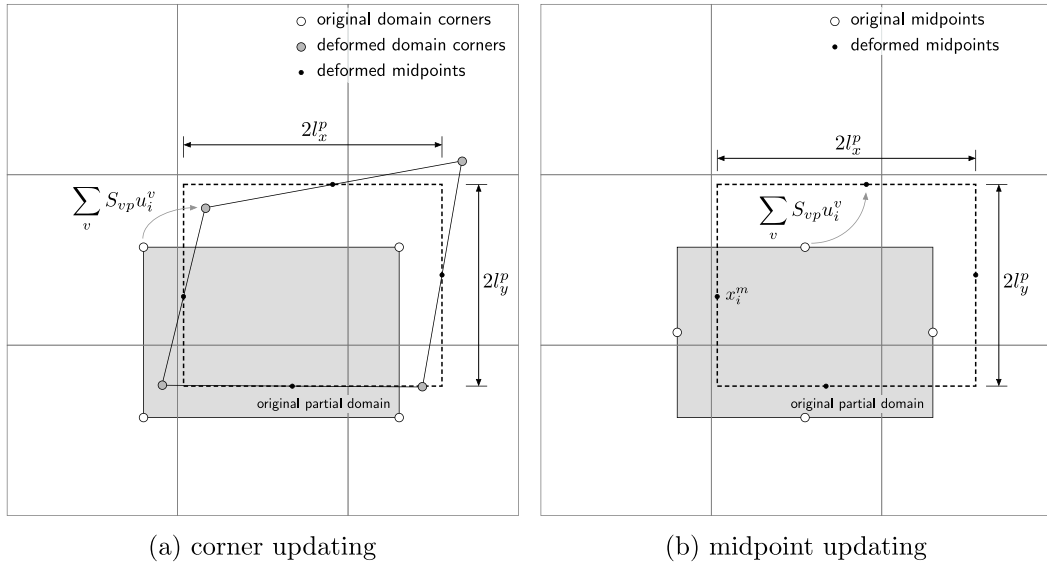


Fig. 5. General domain updating procedures.

$\|(\cdot)\|$ denotes the L2 norm of (\cdot) , $\{f^{ext}\}$ includes the external forces applied to the problem (body forces, tractions, point loads) and $\{f^{react}\}$ are the reaction forces due to the prescribed displacement boundary conditions.

7.1. Compaction under self weight

The first example is an elastic column compressed under its own weight. Initially the column had a height of $l_0 = 50$ m and a width linked to the size of the background grid used to analyse the problem such that there was always one element in the horizontal direction. A plane strain assumption was set in the third direction. The base of the column was restrained vertically and both sides of the column were restrained in the horizontal direction. The column had a Young’s modulus of 1MPa and Poisson’s ratio of zero and a density of $\rho_0 = 80\text{kg/m}^3$. A body force of -800N/m^3 was applied in the vertical (Z, z) direction over 20 equal loadsteps.

The analytical solution for the vertical Cauchy stress is

$$\sigma_{zz}^a = \rho_0 g (l_0 - Z), \tag{41}$$

where g is the gravitational acceleration (taken to be 10 m/s^2), l_0 is the initial height of the column and Z is the initial vertical position within the column. If Poisson’s ratio is zero the stresses in the horizontal directions are equal to zero when the behaviour is elastic.

The convergence behaviour of the standard material point method with different numbers of material points per initially active background grid cell is shown in Fig. 6, where the dimensionless error is defined as

$$\text{error} = \sum_{p=1}^{n_p} \frac{\|(\sigma_p)_{zz} - \sigma_{zz}^a(Z_p)\| V_p^0}{(\rho_0 g l_0) V_0}. \tag{42}$$

In the above n_p is the total number of material points, $(\sigma_p)_{zz}$ is the Cauchy stress in the vertical direction at a material point, Z_p is the material point’s original position, V_p^0 is the original volume associated with the material point and σ_{zz}^a is the analytical Cauchy stress solution in the vertical direction, given by (41). The denominator of (42) is the product of the vertical Cauchy stress at the base of the column multiplied by the column’s original volume, V_0 .

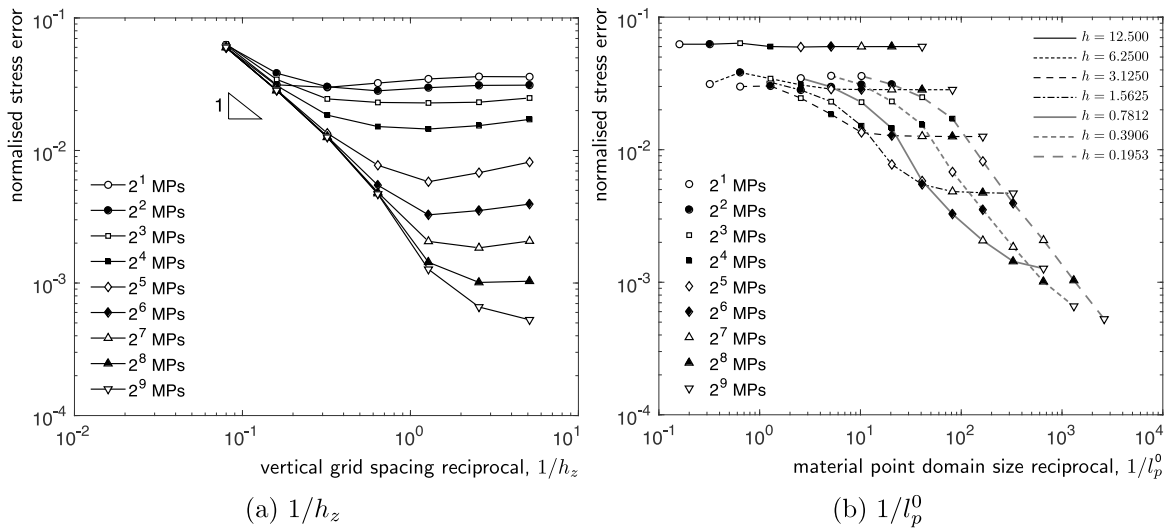


Fig. 6. Elastic compaction under self weight: convergence behaviour with grid and material point refinement for the standard material point method.

Fig. 6 presents the convergence data in two ways: (a) in terms of the normalised stress error against $1/h_z$ for different numbers of material points per background grid and (b) against $1/l_p^0$ with the data points being linked by the size of the background grid.⁷ While it has been reported in the literature that the standard material point method does not converge for this problem due to cell crossing instabilities [21,26]. Fig. 6 shows this is not the case, but in order to achieve continued convergence with grid refinement a large number of material points is required. For this problem the required minimum number of material points per element in the vertical direction appears to be linked to

$$n_p^e \propto \frac{1}{h^2}.$$

For example for $h_z = 1.5625$ m and $h_z = 0.7812$ m approximately 64 and 256 material points per element are required, respectively. This can be seen in Fig. 6 (a) by the 2^6 and the 2^8 lines beginning to stagnate at this point.

For a given background grid size, it can be seen if sufficient material points have been used by the lines that link the discrete data points in Fig. 6 (b). These lines link together common background grid sizes and sufficient material points have been used if the error remains constant with increasing $1/l_p^0$. It is clear that for $h_z = 0.3906$ m and $h_z = 0.1953$ m insufficient material points have been used for the background grid size and for these analyses it is predicted that 1,024 and 4,096 material points per element are required to minimise the error.

Fig. 7 shows the convergence of the CPDI2 and generalised interpolation material point methods with two material points in the vertical direction per initially populated background grid cell. For the generalised interpolation method different domain updating methods are included. When the domains are not updated or when the domains are updated according to the determinant of the deformation gradient (32), the method fails to converge beyond the third and sixth analyses, respectively. However, when the domains are updated according to (33), (34) or (37) the method continues to converge with background grid refinement at the same rate as the CPDI2 method.

The method fails to converge when the domains are not updated due to the physical change in volume due to compaction under self weight not being accounted for at the material points, resulting in an over-stiff response. When the domains are updated according to (32) they contract in the horizontal direction due to the vertical compression. This causes a spurious reduction in the overlap between the background grid elements and the material point's domain and insufficient compression of the domain in the vertical direction. The result of this is that the method fails to converge towards the correct analytical solution beyond the sixth refinement step.

⁷ As the standard material point method is used in this example the length of the material point domains are obtained by assuming $l_p^0 = \sqrt{V_p^0}/2$.

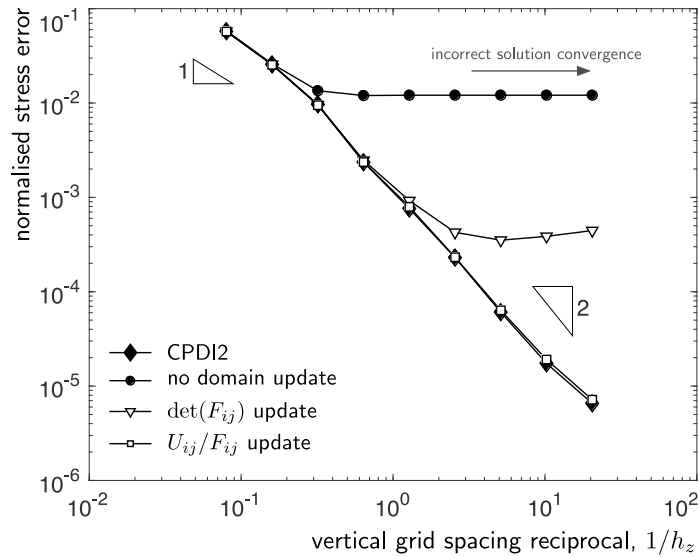


Fig. 7. Elastic compaction under self weight: convergence of different generalised interpolation material point domain updating methods with grid refinement for 2² material points per element.

Fig. 8 shows the vertical stress versus deformed position response with different domain updating methods with $h_z = 1.5625$ m but with a reduced Young’s Modulus of $E = 10$ kPa such that the height of the column at the end of the analysis should be approximately 24m. The three inset figures on the right of Fig. 8 show the material point domains at the end of the analysis. The domains have been coloured according to the point’s vertical stress, σ_{zz} . The grey dashed line shows the lower limit of the physical domain, $z = 0$, and the background grid is also shown by the fine solid lines. The overlaps in the material point domains for the case where the domains are not updated causes the over-stiff response shown in Fig. 8. The stress oscillations at the base of the column when the domains are not updated and when the domains are updated according to $\det(F_{ij})$ are caused by the bottom material point domains exceeding the physical problem domain. This can also be seen by the domain colouring on the insert figures.

7.2. Simple shear

The second example is a plane strain unit square subjected to simple shear with elastic and elasto-plastic material behaviour. The updated coordinates and deformation gradient for this problem are

$$\{x\} = \begin{Bmatrix} X + (\Delta l/l_0) \times Y \\ Y \\ Z \end{Bmatrix} \quad \text{and} \quad [F] = \begin{bmatrix} 1 & \Delta l & 0 \\ 0 & 1 & 0 \\ 0 & 0 & 1 \end{bmatrix},$$

where $\det([F]) = 1$, l_0 the original height of the domain and Δl the top face shearing distance (as shown in Fig. 9). For the elasto-plastic analysis yielding of the material was governed by a von Mises yield function of the form

$$f = \rho - \rho_y = 0, \tag{43}$$

where $\rho = \sqrt{2J_2}$, $J_2 = s_{ij}s_{ji}/2$, $s_{ij} = \tau_{ij} - \tau_{kk}\delta_{ij}/3$ and ρ_y is the deviatoric yield stress of the material. The unit square had a Young’s modulus of 10 kPa and Poisson’s ratio of 0.3 and a density of $\rho_0 = 0$. The top surface of the 1m square was sheared by $\Delta l = 6$ m over 30 equal displacement controlled loadsteps. The shearing was imposed on all of the background cells that contained the outer boundary of material points, as shown by the black-filled circles in Fig. 9.

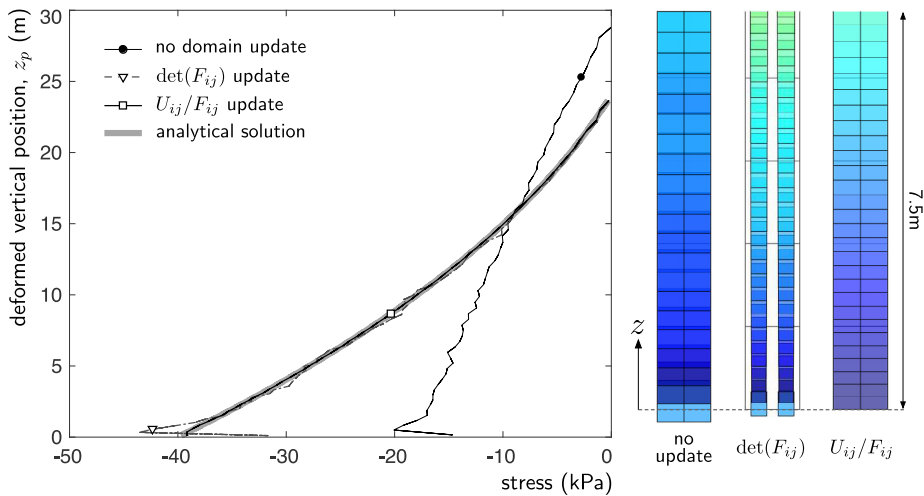


Fig. 8. Elastic compaction under self weight: vertical stress versus position for different domain updating methods with $E = 10$ kPa and $h_z = 1.5625$ m. (For interpretation of the references to colour in this figure legend, the reader is referred to the web version of this article.)

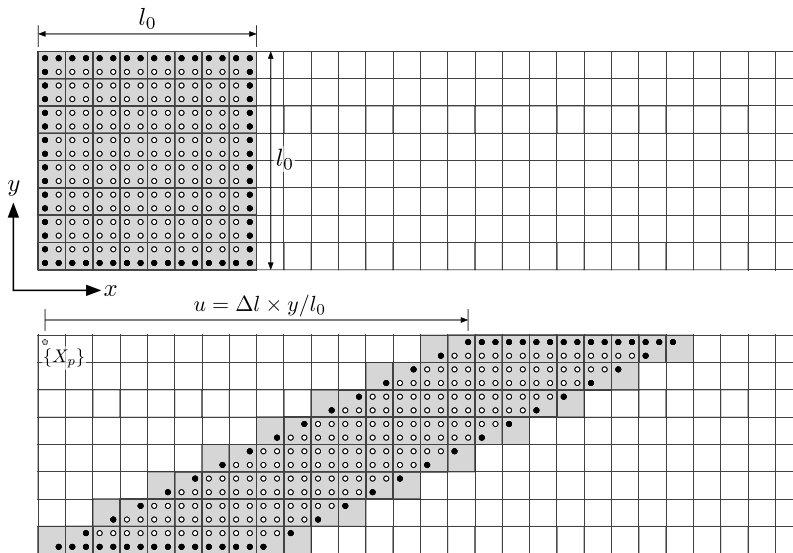


Fig. 9. Simple shear: problem geometry with $l_0 = 1$ m, $h = 0.125$ m and 2^2 material points per initially active background elements. Boundary material points are shown by the black-filled circles. The bottom figure shows the deformed material point positions and the active elements for $\Delta l = 2$ m.

The normalised stress versus deformation response for an analysis using the standard material point method with $h = 0.125$ m and 3^2 material points per initially active background grid cell is shown in Fig. 10 with (a) elastic and (b) elasto-plastic material behaviour with $\rho_y = 5$ kPa. This is a constant stress problem and all of the material points have the same stress response (to machine precision). The analytical solution for elastic behaviour is shown by the solid grey line in Fig. 10 (a) and the material point solution agrees with this solution to a normalised error of the order of 1×10^{-5} . As this is a constant stress problem, the standard material point method does not suffer from the cell crossing problems in the previous example.

The standard, generalised interpolation and CPDI2 material point methods predict the correct response for the constant stress problem. The only exception was when the domains were updated according to the stretch tensor,

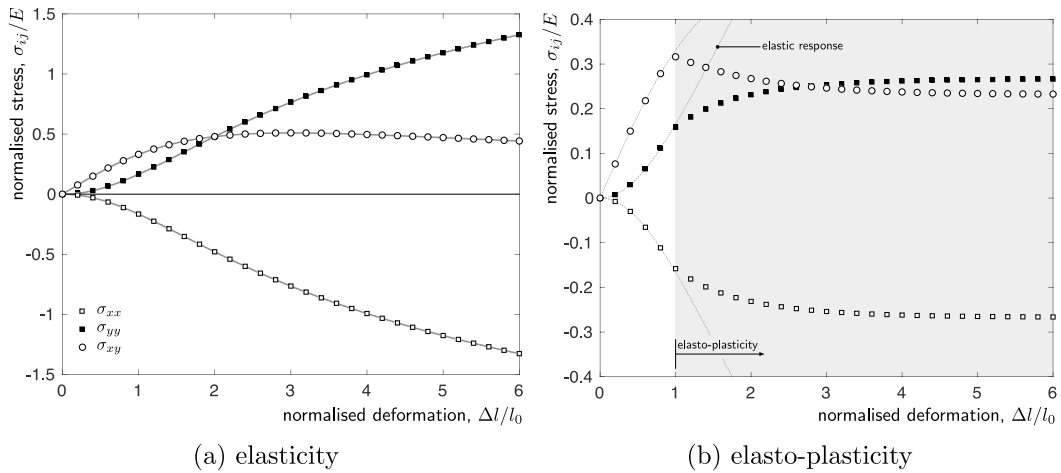


Fig. 10. Simple shear: normalised stress versus deformation material point response (discrete points) and analytical solution (solid grey line).

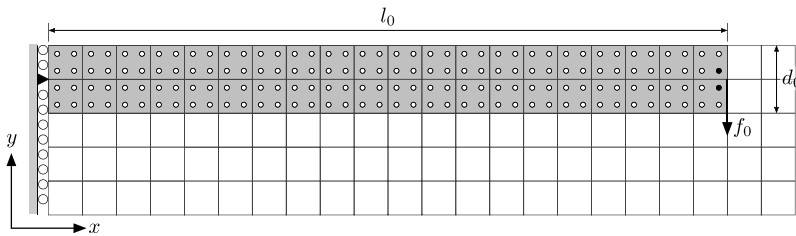


Fig. 11. Elastic beam: problem geometry and boundary conditions with $h = 0.5$ m and 2^2 material points per initially active background elements.

U_{ij} , through (34), as explained in Section 6.4. This domain updating method introduces spurious volume changes and domain expansion/contraction under pure shear which should be an isochoric deformation field. The expansion of the domains in the vertical direction causes the areas associated with the top and bottom layer of material points to go beyond the boundary of the physical problem, losing partition of unity of the basis functions and causing a spurious variation in the stress field.

7.3. Elastic cantilever beam

The third example is a plane strain analysis of an elastic beam subjected to a vertical end load of 100kN applied over 50 equal loadsteps. The beam had an initial length $l_0 = 10$ m and depth $d_0 = 1$ m and the material had a Young’s modulus of 12MPa and a Poisson’s ratio of 0.2. The geometry and boundary conditions with $h = 0.5$ m and 2^2 material points per initially active background elements is shown in Fig. 11. The force was split across the two material points closest to the neutral axis at the end of the beam (the black-filled circles in Fig. 11). The neutral axis of the beam was pinned at its left hand edge and roller boundary conditions were imposed on the other background grid nodes at the root of the beam, as shown in Fig. 11.

The deformed material point positions coloured according to the Cauchy stress in the horizontal direction, σ_{xx} , for loadsteps 4, 8, 16 and 50 (top to bottom) with $h = 0.5, 0.25$ and 0.125 m (left to right) and 2^2 standard material points per initial background element are shown in Fig. 12. In each case the active background elements are shaded grey. It is clear from the figure that this is a very large deformation problem with the beam deforming vertically by almost its original horizontal length. Most of the vertical deformation occurs in the first 20 loadsteps. After this

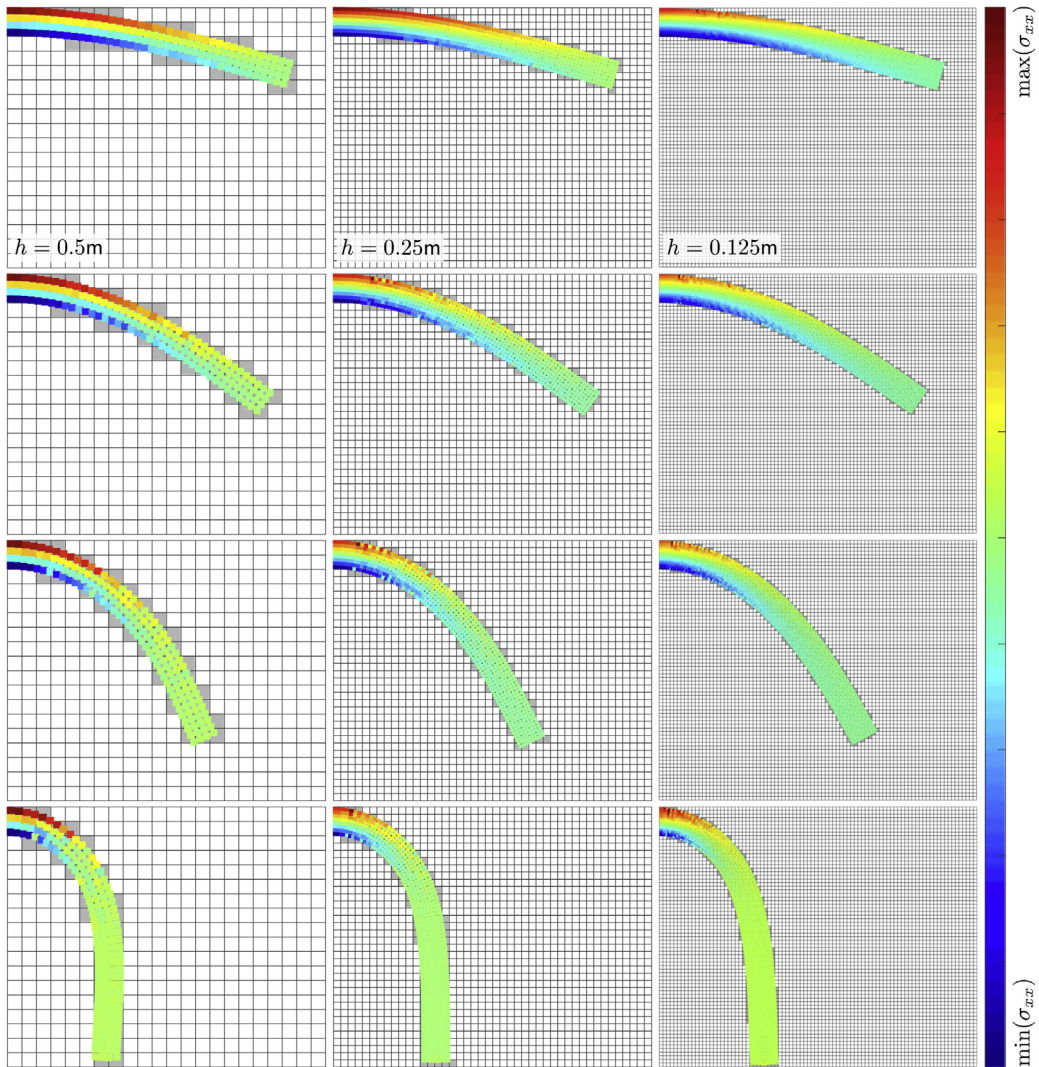


Fig. 12. Elastic beam: deformed material point positions coloured according to σ_{xx} for loadsteps 4, 8, 16 and 50 (top to bottom) with $h = 0.5, 0.25$ and 0.125m (left to right) and 2^2 material points per initial background element. The active background grid cells have been shaded grey. (For interpretation of the references to colour in this figure legend, the reader is referred to the web version of this article.)

point the structural action of the beam transfers from acting in bending to acting as a tie with a significant stiffening of the global response.

The normalised horizontal and vertical displacement versus normalised force response for different background grid sizes and numbers of material points are shown in Fig. 13. The displacements have been normalised by the original length of the beam, l_0 , and the force by the maximum applied force of 100kN. Fig. 13 (a) shows the force–displacement response for $h = 0.5\text{ m}$ and $3^2, 6^2, 9^2$ and 12^2 material points per initially active background grid cells.⁸ The analytical solution of [33] is shown by the discrete points with the horizontal and vertical solutions being shown by the black- and white-filled circles, respectively. Increasing the number of material points reduces the oscillations in the force–displacement response and the global response curves converge with increasing numbers of material points. The oscillations are caused by the sudden transfer of force and stiffness between background grid

⁸ The total numbers of material points is given by $10 \times n^2/h^2$, where n is the number of material points in each direction in the element.

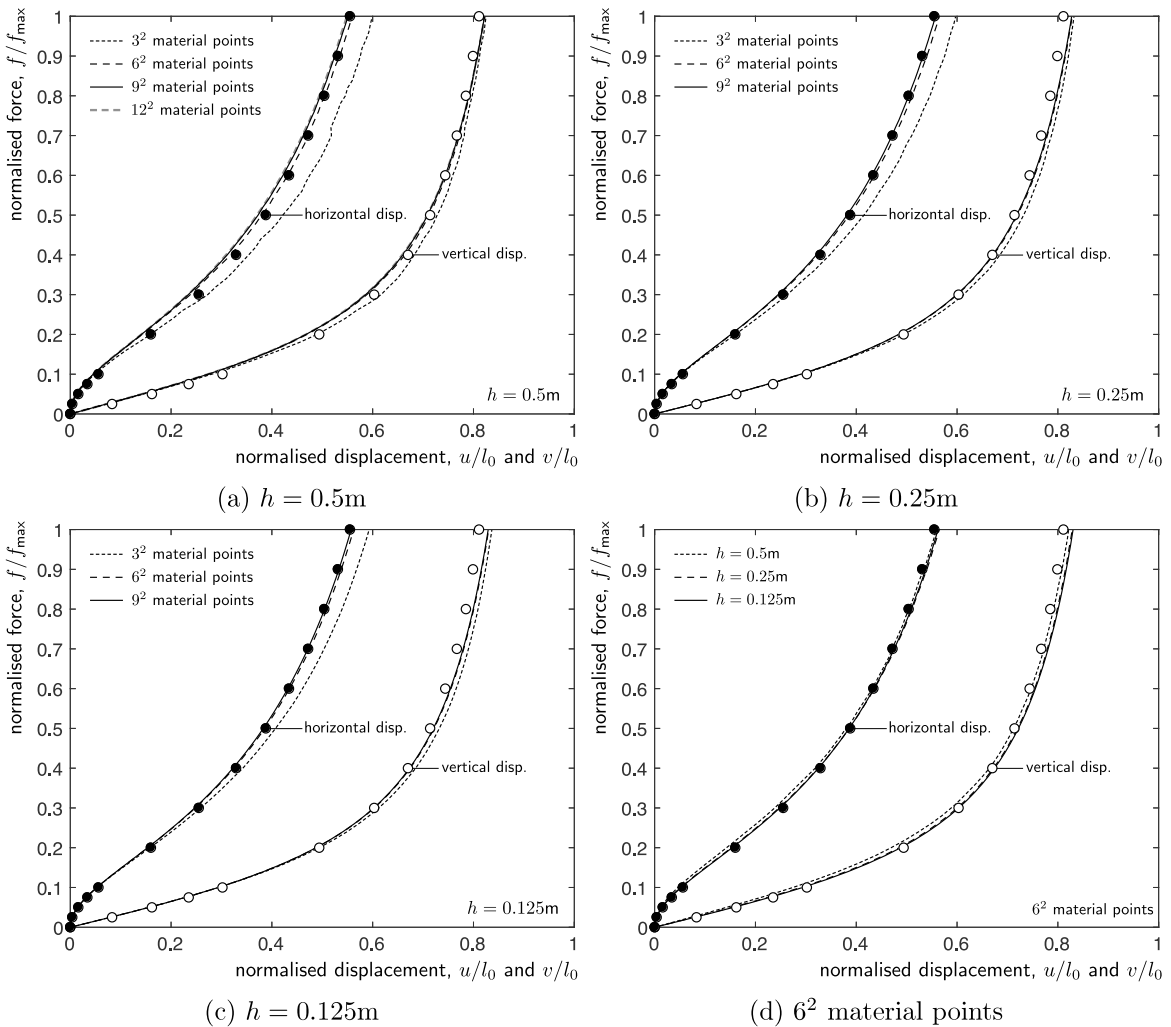


Fig. 13. Elastic beam: normalised force versus horizontal and vertical displacement response for the standard material point method. The analytical horizontal (black-filled circles) and vertical (white-filled circles) solution of [33] is also shown.

cells as material points cross between background grid cells. Increasing the number of material points increases the instances of cell crossing but each of the material points has a lower volume resulting in a more gradual transfer of force and stiffness. Similar behaviour is seen in Fig. 13 (b) and (c) with background grid sizes of $h = 0.25$ m and $h = 0.125$ m, respectively. Fig. 13 (d) shows the response of mesh sizes $h = 0.5$ m, $h = 0.25$ m and $h = 0.125$ m with 6^2 material points per initially active background grid element. There is little difference between the force–displacement responses and the number of material points appears to be more important than the background grid size for this analysis.

Fig. 14 shows the deformed material point positions coloured according to σ_{xx} for $h = 0.25$ m with different numbers of material points. In particular the figure shows the detail of the stress field around the root of the cantilever. It is clear from the figure that increasing the numbers of material points reduces the oscillations in the stress field. However, oscillations are still present at material points which are located in very sparsely populated elements (very little physical volume relative to the size of the element); two of these points have been identified by the black-dashed circles for 6^2 material points. The remaining oscillations are due to the basis functions of the underlying background mesh being unable to capture the stress variation through the beam.

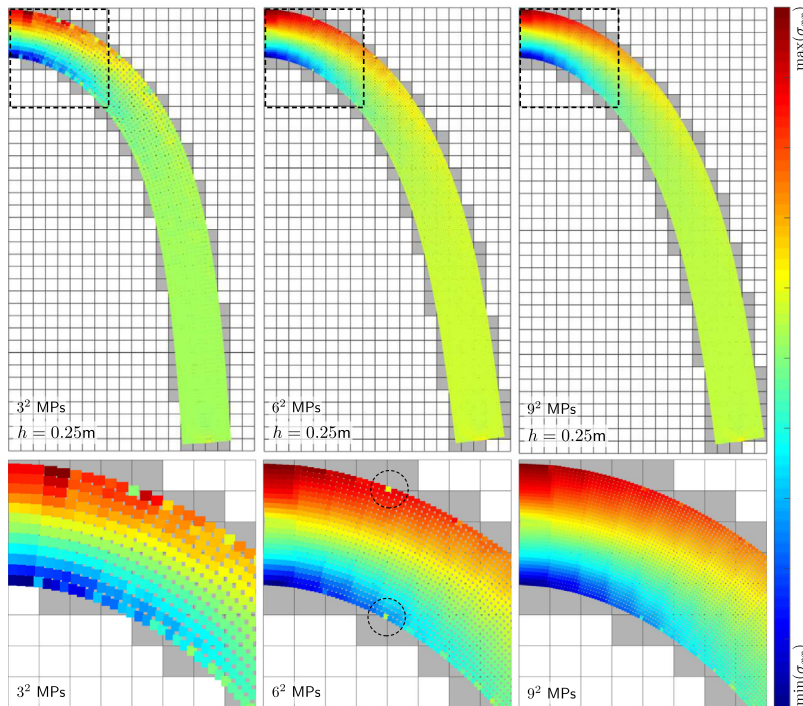


Fig. 14. Elastic beam: deformed material point positions coloured according to σ_{xx} for $h = 0.25$ m. The *active* background grid cells have been shaded grey. (For interpretation of the references to colour in this figure legend, the reader is referred to the web version of this article.)

The force versus displacement response of the generalised interpolation material point method is shown in Fig. 15 for: (a) different background grid sizes and (b) for different domain updating methods with $h = 0.5$ m, all with 6^2 points per initially populated elements. As with the standard material point method, changing the grid size has little influence on the force–displacement response when sufficient material points are used. The different domain updating methods give very similar responses, except in the case where the domains are updated according to the normal components of the deformation gradient (32). In this case, due to the large rotation of the beam, the material point domains artificially shrink and the force–displacement response deviates from the correct solution after approximately 15% of the load has been applied and fails to converge beyond load step 19 (highlighted by the grey-filled circles in Fig. 15 (b)). Similar behaviour of the (32) updating method was shown in Charlton et al. [21].

Fig. 16 shows the deformed generalised interpolation material point positions coloured according to σ_{yy} for 6^2 material points per initial grid cell and $h = 0.5, 0.25$ and 0.125 m background grid sizes. In these analyses the material point domains were updated according to (37) (volume-corrected corner update with mid-side determination). The detail around the loaded end of the cantilever beam is shown for $h = 0.125$ m which clearly shows the stress concentration caused by loading the two mid-depth material points (enclosed by the dashed-circular line, A). This stress concentration causes the over estimation of the vertical displacement shown in Figs. 13 and 15.

Fig. 17 shows the normalised force versus displacement response of the CPDI2 method with 3^2 material points per initially populated background grid cell. The response is very similar to that of the generalised interpolation material point method provided that an appropriate domain update procedure is adopted.

Table 3 shows the equilibrium convergence of the generalised interpolation material point method with $h = 0.125$ and 6^2 material points per element. The out of balance force residual (40) is shown for loadsteps 10, 20, 40, 49 and 50 with the other loadsteps having a similar response. In all cases asymptotic quadratic convergence is achieved as the algorithm approaches equilibrium satisfaction. This can be seen by the negative exponent on the residual

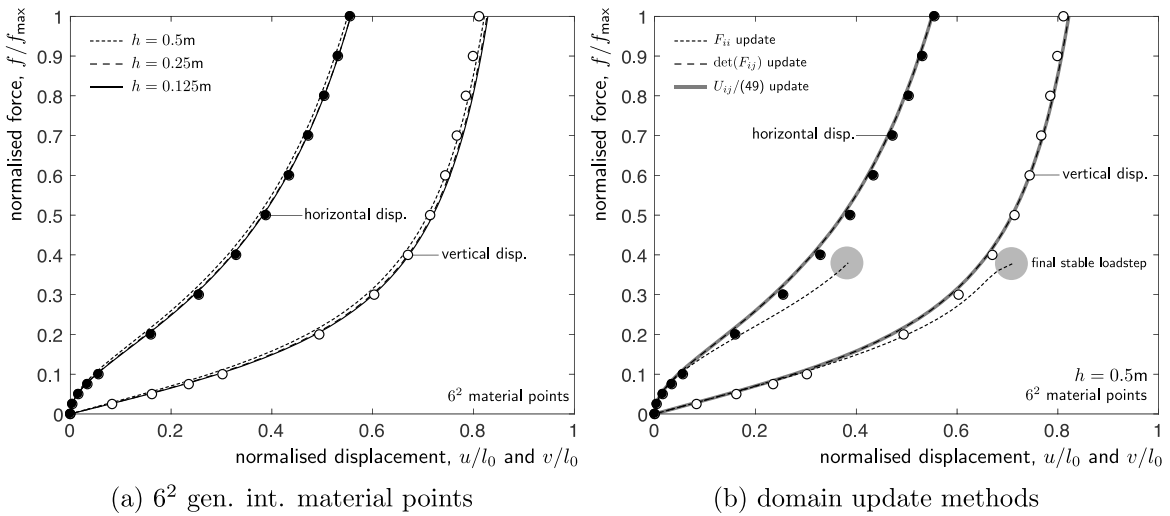


Fig. 15. Elastic beam: normalised force versus horizontal and vertical displacement response for the generalised interpolation material point method. The analytical horizontal (black-filled circles) and vertical (white-filled circles) solution of [33] is also shown.

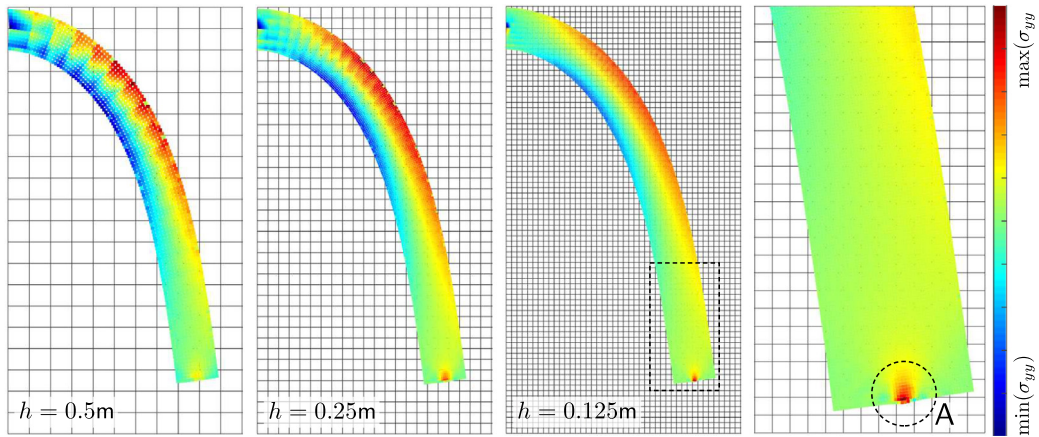


Fig. 16. Elastic beam: deformed generalised interpolation material point positions coloured according to σ_{yy} for 6^2 material points per initial grid cell and three different background grid sizes. Detail is shown around the end of the beam for $h = 0.125$ m. (For interpretation of the references to colour in this figure legend, the reader is referred to the web version of this article.)

doubling with between iterations. This verifies the derivation of the previously converged consistent tangent (A.3) and its implementation within the generalised interpolation material point methods for large strain elasticity.

Table 4 presents the normalised run times and total number of N–R iterations for the standard, generalised interpolation and CPDI2 material point methods where the run times have been normalised with respect to the finite element run time with $h = 0.5$ m. All of the material point analyses used 6^2 material points per initially populated element and the material point method implementation was based on [34]. The reference finite element code was taken from Coombs et al. [35], with four-noded bi-linear quadrilateral elements integrated using 6^2 integration

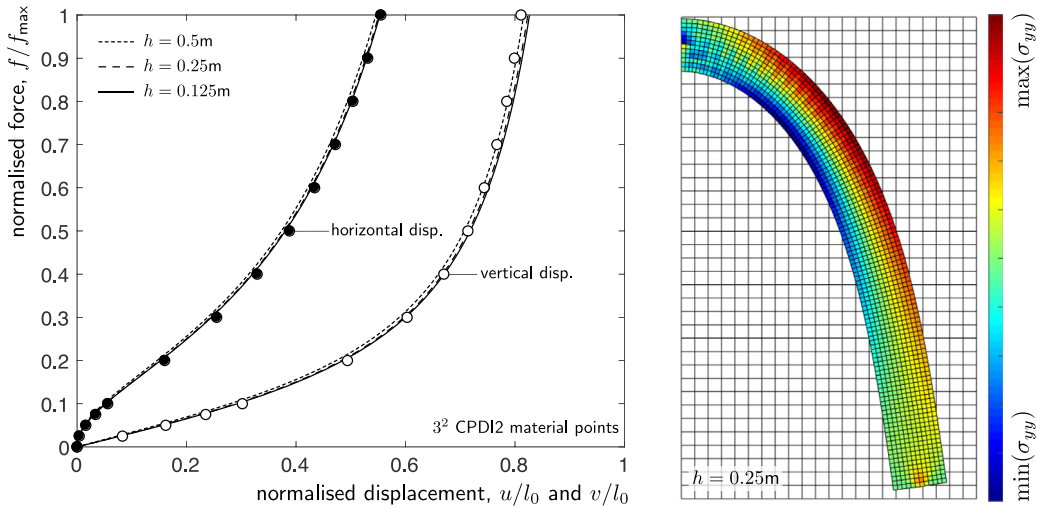


Fig. 17. Elastic beam: normalised force versus horizontal and vertical displacement response for the CPDI2 material point method with 3^2 points per initially populated background grid cell. The analytical horizontal (black-filled circles) and vertical (white-filled circles) solution of [33] is also shown.

Table 3

Elastic beam: generalised interpolation material point method equilibrium residual (40) for loadsteps 10, 20, 40, 49 and 50 with $h = 0.125$ and 6^2 material points per element.

NR it.	Load step				
	10	20	40	49	50
0	$1.622 \times 10^{+1}$	$1.107 \times 10^{+1}$	8.740×10^0	6.774×10^0	6.901×10^0
1	1.242×10^{-1}	1.699×10^{-2}	1.731×10^{-3}	1.509×10^{-3}	9.246×10^{-4}
2	2.436×10^{-4}	1.366×10^{-5}	2.890×10^{-6}	1.072×10^{-5}	2.112×10^{-6}
3	5.524×10^{-5}	3.660×10^{-7}	1.131×10^{-10}	1.089×10^{-9}	5.012×10^{-11}
4	1.470×10^{-10}	9.912×10^{-15}	–	3.250×10^{-15}	–

Table 4

Elastic beam: normalised run times and total number of N–R iterations (in brackets) for different material points methods. The run times have been normalised by the $h = 0.5$ m finite element method (FEM) run time and all analysis use 6^2 material points, or integration points, per initially populated element.

Mesh	MPM	GIMP	CPDI2	FEM
$h = 0.500$ m	1.11 (210)	1.16 (214)	1.08 (205)	1.00 (157)
$h = 0.250$ m	5.60 (210)	5.47 (218)	5.04 (202)	3.91 (155)
$h = 0.125$ m	32.54 (215)	34.23 (227)	32.07 (202)	15.85 (154)

points per element such that the total number of integration points matched the total number of material points.⁹ All analyses were conducted using MATLAB R2017b within a macOS V.10.14.5 environment on a 2.3 GHz Intel Core i7 with 16GB of RAM. For the coarsest analyses ($h = 0.5$ m) the material point run times are between 8% and 16% longer than that of the equivalent finite element analysis. The variation in the different material point methods is mainly due to the different number of global N–R iterations required to find convergence, as shown by the bracketed numbers in Table 4. As the problem is refined the run times for the finite element analysis and the

⁹ We acknowledge that this is in excess of what is required to integrate a bi-linear quadrilateral element, however it provides a fairer comparison between the numerical methods by eliminating one of the variations between the different approaches.

Table 5

Elastic beam: run time distribution for the standard material point method with $h = 0.5$ m and 6^2 material points per element. The grey-shaded cells are sub calculations of the numbered entries.

Calculation	Calls	Run time
1. Background grid stiffness & internal force	211	79.8%
– Material stiffness, \tilde{A}_{ijkl}	303,840	32.5%
– Constitutive model	303,840	5.3%
2. Element–material point information	50	16.6%
– Element–material point search	50	6.4%
– Basis functions	288,000	5.5%
– Material point–node list	72,000	1.3%
3. Material point update	50	1.8%
4. External force	50	1.0%
5. Linear solver	211	0.1%
6. Other	–	0.7%

material point methods increase at different rates. This is due to the structure of the implemented material point code being different from the finite element method, specifically that in the material point code the primary loop is over material points rather than elements in the finite element code. It is widely known that MATLAB is inefficient at handling large loops that operate on relatively small amounts of data within each loop execution. This is due to the overheads associated with RAM to cache communication (see [36–38], amongst others, for a detailed discussion on this issue, as well as methods to overcome it). Other differences include that for material point methods, the basis functions (and derivatives) need to be determined at each material point at the start of each load step whereas for the finite element method the basis functions can be determined once at the start of the analysis as the local positions of the integration points do not change.

Table 5 provides a breakdown of the run time for the standard material point method with $h = 0.5$ m and 6^2 material points per element. The majority of the calculation time (almost 80%) is spent in determining the internal force and stiffness of the background grid nodes, (27) and (28), and within this the evaluation of the consistent tangent at each material point, \tilde{A}_{ijkl} , takes over 30% of the total run time for the analysis. This can be attributed to the fact that these calculations must be performed for each material point (1,440 in total) for every N–R iteration (211 in this case) - 303,840 material point evaluations in total. The other major contributor to the total run time is determining the interaction between the background grid and the material points in terms of element–material point searching, basis function calculation and determining a unique list of nodes for each material point. Updating the material points and assembling the external force are minor actions in terms of the run time, whereas the time spent in the linear solver is insignificant.

7.4. Elastic annulus under torsional deformation

The next example is of an elastic annulus with an inner radius of $R_i = 0.75$ m and an outer radius of $R_o = 1.25$ which was subjected to a torsional deformation field where the rotational deformation is dependent on the radial position, R , through

$$\theta = \alpha \left(\frac{16(R - R_i)^2(R - R_o)^2}{(R_i - R_o)^4} \right), \quad (44)$$

where α controls the magnitude of the deformation. The problem is analysed by applying the appropriate body force¹⁰ to cause this rotational deformation, determined via the Method of Manufactured Solutions (MMS). The inner and outer surfaces of the annulus are constrained by homogeneous Dirichlet boundary conditions. The problem is similar to that analysed by Kamojjala et al. [39] and Wang et al. [19]. The material had a Young's modulus of 1Pa and a Poisson's ratio of 0 and was modelled using the standard material point method using an unstructured background grid of linear three-noded triangles. The displacement field and associated body forces are shown in Fig. 18. Although the displacement field is relatively simple, the associated body forces required to cause this displacement field are complex.

¹⁰ See Wang et al. [19] for details of the derivation of the body force for this problem.

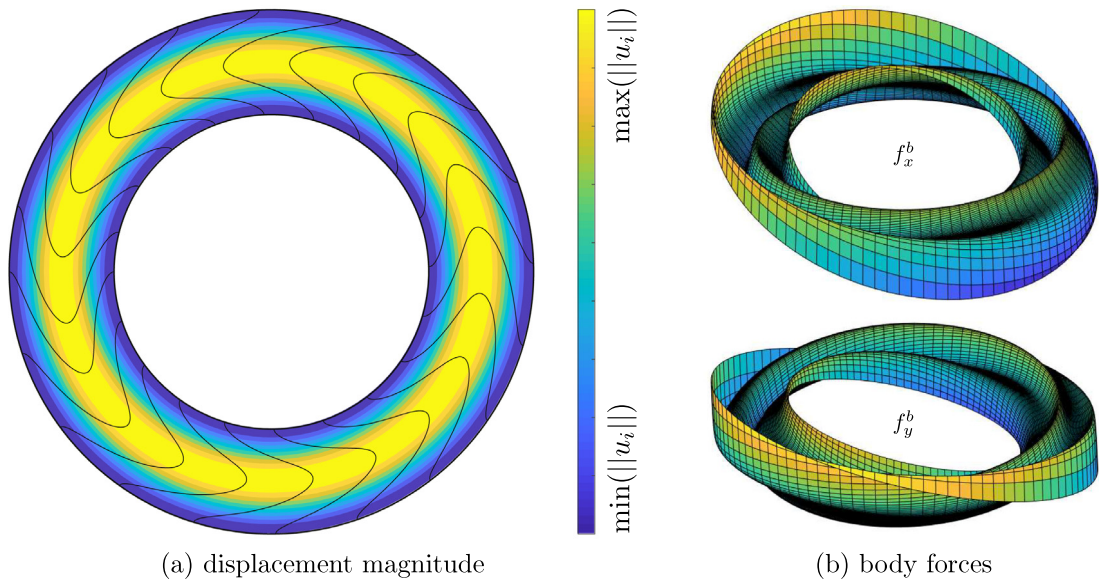


Fig. 18. Elastic annulus: displacement field and body force components. For the body forces the maximum positive and negative values are coloured yellow to blue, respectively. (For interpretation of the references to colour in this figure legend, the reader is referred to the web version of this article.)

The problem was analysed with five different background grid sizes varying between 0.4363m and 0.0273m and 1^2 , 2^2 , 2^3 and 2^4 material points per element. A rotation of $\alpha = 0.1$ radians was applied over 10 equal load steps. For the finest mesh this results in the material points at the midpoint of the annulus displacing 4 times the mesh size.

The convergence of the absolute displacement error with mesh refinement when analysed using the standard material point method is shown in Fig. 19. The convergence behaviour is similar to that shown for the compaction under self weight problem in that, provided that sufficient material points are used, the method approaches the correct convergence rate for the underlying basis. It is also clear that one material point per element is insufficient due to the complex variation in the body force over the domain. The figure also shows three of the background meshes used and the associated displacement magnitude of the material points at the end of the analysis with 2^2 material points per element.

7.5. Elasto-plastic collapse

The final example in this paper is the plane strain collapse of a 16m by 8m block of material with a Young's modulus of 1MPa and a Poisson's ratio of 0.3. Yielding of the material was governed by the von Mises yield criterion, (43), with $\rho_y = 20$ kPa. Due to symmetry only half of the problem was modelled and roller boundary conditions were imposed on the base and the left hand edge of the background grid. The problem geometry and boundary conditions with $h = 1$ m and 2^2 material points per initially active background is shown in Fig. 20, where $l_0 = 8$ m. A body force of $-10,000\text{N/m}^3$ was applied in the vertical, y , direction over 40 loadsteps.

Fig. 21 shows the deformed material point positions coloured according to the vertical stress, σ_{yy} , for different background grid sizes ($h = 2, 1, 0.5$ and 0.25m) and numbers of material points per initially populated grid cell (3^2 , 6^2 and 9^2 points per element). With coarse meshes, especially with low numbers of material points per initially populated element, there are severe stress oscillations through the body. These reduce with background and the material point refinement, however oscillations between adjacent elements still exist due to the combination of cell crossing and discontinuous spatial derivatives of the basis functions. Some authors, e.g. Wang et al. [40],

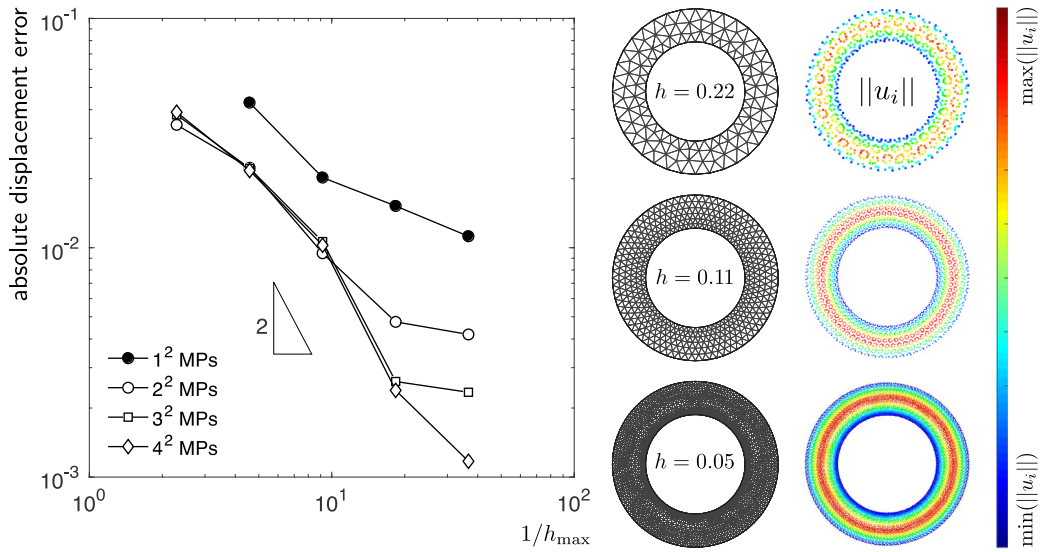


Fig. 19. Elastic annulus: absolute displacement error convergence with mesh refinement for different numbers of material points. Three different mesh sizes and rotational deformation fields are shown for 2^2 material points per element.

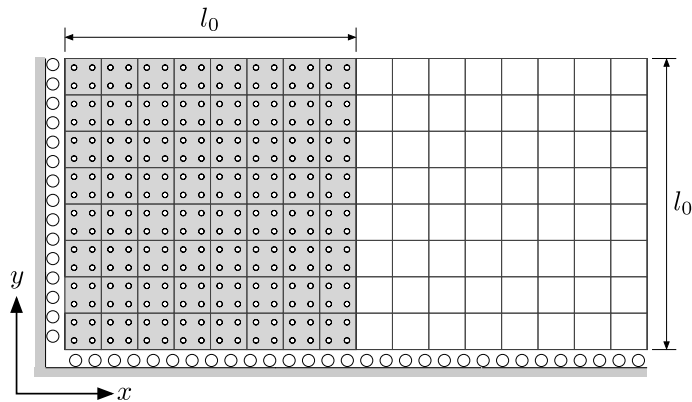


Fig. 20. Elasto-plastic collapse: problem geometry and boundary conditions with $h = 1$ m and 2^2 material points per initially active background elements (grey-shaded).

have combined the material point method with a plastic strain-driven softening constitutive relationship to model progressive slope failure. Although the distribution of the progressive failure segments appear to be physically realistic it is likely that they are triggered by the grid-aligned stress oscillations and, as with other localisation problems, will be highly mesh dependent.

Table 6 gives the final extent and maximum height of the collapse using the standard material point method with different background grid sizes and numbers of material points per initially populated background grid cell. The extent and height converge with both grid and material point refinement. However, unlike with the elastic beam analysis the dominant factor is the grid spacing, h , and for finer meshes changing the number of material points from 6^2 to 9^2 has little influence on the final result.

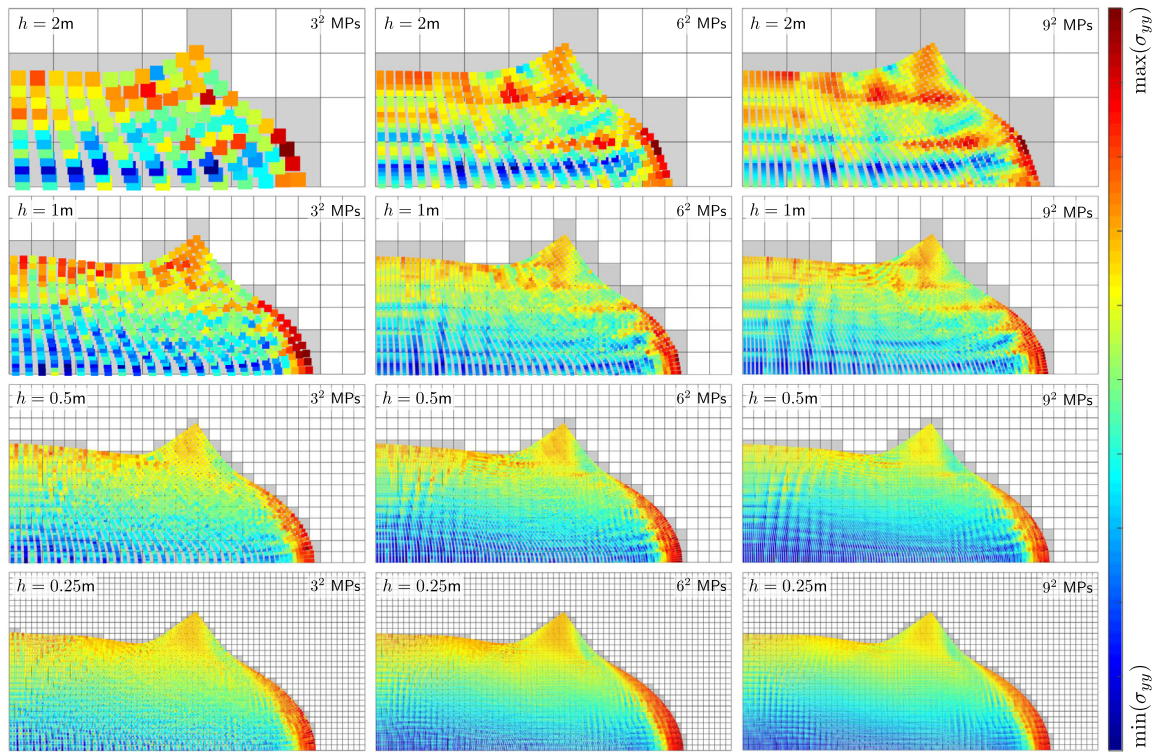


Fig. 21. Elasto-plastic collapse: deformed material point positions coloured according to σ_{yy} . (For interpretation of the references to colour in this figure legend, the reader is referred to the web version of this article.)

Table 6

Elasto-plastic collapse: collapse extent and height (m) with different background grid sizes and numbers of material points per element.

nMPs	Horizontal extent				Maximum height			
	$h = 2.0$	$h = 1.0$	$h = 0.5$	$h = 0.25$	$h = 2.0$	$h = 1.0$	$h = 0.5$	$h = 0.25$
3^2	13.343	13.662	13.731	13.787	6.357	6.245	6.245	6.234
6^2	13.359	13.735	13.797	13.847	6.437	6.277	6.251	6.231
9^2	13.380	13.750	13.812	13.863	6.452	6.289	6.255	6.226

Fig. 22 shows the deformed generalised interpolation material point domains coloured according to the vertical stress, σ_{yy} , for $h = 1$ m and 6^2 material points per initially populated background grid cell with different domain updating methods. The figure also shows the result of the CPDI2 method, which serves as a reference point for the different domain updating methods. Updating the domains according to the determinant of the deformation gradient (32) causes the domains to shrink artificially in the horizontal direction due to the vertical compression of the material. They also do not contract sufficiently in the vertical direction resulting in domains at the bottom of the problem moving beyond the background mesh. This causes a loss of partition of unity for those points and elevated the stresses at the base of the domain. As with the beam problem, if the domains are updated according to the normal components of the deformation gradient, (33), material points that experience large rotations spuriously shrink (as shown by the points in the dashed circle in Fig. 22 (b)). This results in a softer response compared to the other domain updating methods, as shown by the maximum extent and height values given in Table 7. This issue is removed by the volume-corrected deformation gradient update (38) or (39) which gives similar extent and

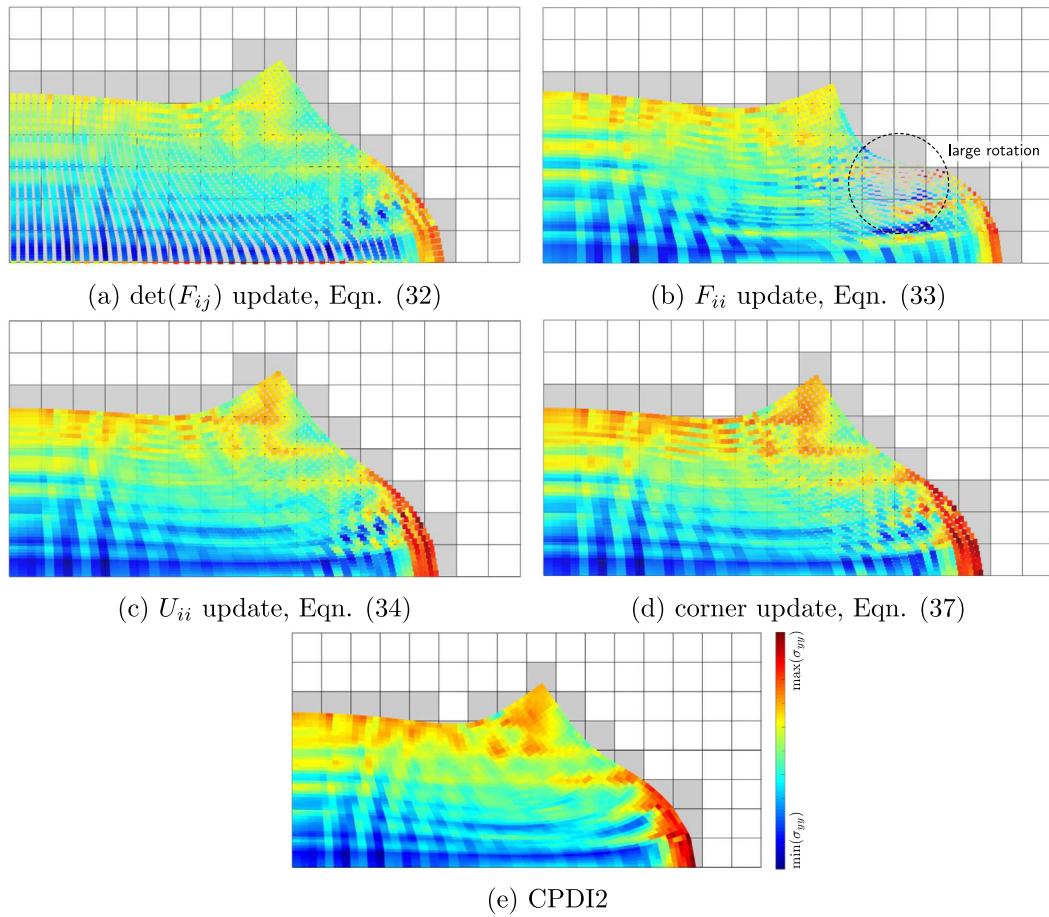


Fig. 22. Elasto-plastic collapse: (a)–(d) deformed generalised interpolation material point positions with different domain updating methods and (e) CPDI2. All analyses use $h = 1$ m and 6^2 material points per element. The domains are coloured according to σ_{yy} , the most compressive and tensile stresses are blue and red, respectively. (For interpretation of the references to colour in this figure legend, the reader is referred to the web version of this article.)

maximum height values as the (34) and (37) domain updating methods as well as the CPDI2 method. Despite using generalised interpolation and CPDI2 material point methods, significant stress oscillations are still evident. Based on the findings of [26], it is unlikely that the oscillations are due to volumetric locking, instead they are a consequence of the bi-linear background grid. In the material point method the stress field is composed of the incremental summation of element contributions over a number of load (or time) steps. The variations in stress seen in Fig. 22 are due to the underlying basis of the finite element grid being unable to represent the stress field variation, rather than a manifestation of grid crossing. This is particularly evident on the right hand edge of the domain where the material points have moved, and crossed elements, horizontally. The stress variation within these elements clearly tracks to the background cell boundaries, with almost no variation in the vertical stress profile within the base elements which is consistent with the spatial derivatives of the background mesh.

The equilibrium convergence of the generalised interpolation material point method with $h = 1$ m and 6^2 material points per element is shown in Table 8 for loadsteps 10, 20, 30 and 40. Although in some cases the global iterations take a number of iterations to find the correct descent path, once approaching the correct solution asymptotic quadratic convergence is achieved. This verifies the consistent derivation and implementation of the consistent tangent for the previously converged Lagrangian formulation with large strain elasto-plasticity.

Table 7

Elasto-plastic collapse: collapse extent and height with the generalised interpolation and CPDI2 methods with $h = 1$ m and 6^2 material points.

	Domain updating method					CPDI2
	Eq. (32)	Eq. (33)	Eq. (34)	Eq. (37)	Eq. (38)/(39)	
Horizontal extent (m)	13.645	14.415	13.425	13.769	13.769	13.780
Maximum height (m)	6.316	5.546	6.441	6.392	6.257	6.292

Table 8

Elasto-plastic collapse: generalised interpolation material point method equilibrium convergence for loadsteps 10, 20, 30 and 40 with $h = 1$ m and 6^2 material points per element.

NR it.	Load step			
	10	20	30	40
0	2.656e+00	2.794e+00	2.701e+00	2.410e+00
1	2.697e-04	3.088e-02	2.380e-02	1.759e-02
2	1.626e-09	2.410e-02	4.626e-02	3.049e-02
3	6.057e-15	2.568e-03	6.193e-03	5.156e-03
4	–	3.910e-05	2.225e-04	1.497e-04
5	–	6.949e-10	1.356e-07	1.944e-07
6	–	–	6.713e-14	3.159e-13

7.6. Observations

This section has presented the analysis of five large deformation problems using the previously converged Lagrangian formulation of the material point method. The examples have verified the formulation and its implementation through convergence towards analytical solutions and through obtaining the correct equilibrium rates of convergence, respectively. The following observations can be made from the analyses presented in this section:

1. *Compaction under self weight*: this simple large deformation problem highlighted issues associated with different generalised interpolation domain updating methods and, in this case, only (33), (34) and (37) are appropriate choices to achieve continued convergence. It has also shown that excessive numbers of material points are required to minimise the errors associated with cell crossing when using the standard material point method.
2. *Simple shear*: all of the material point methods predict the correct response for this problem. As the stress, strain, and material stiffness do not vary spatially within the problem domain there are no cell-crossing instabilities. The only method that did not predict the correct response was when the domains of the generalised interpolation material point method were updated according to the stretch tensor, U_{ij} , through (34).
3. *Elastic cantilever beam*: results of this analysis are not highly dependent on the grid size provided that sufficient material points were used (above 6^2 material points per initially populated element). Low numbers of material points cause spurious stress oscillations through the beam. Applying the end load as a concentrated force on material points immediately above/below the neutral axis leads to an overestimation of the vertical displacement due to a local stress concentration. If the generalised interpolation material point domains are updated according to the normal components of the deformation gradient, F_{ii} , through (32) the domains artificially shrink, due to large rotation components in the deformation gradient, and the method fails to complete the analysis.
4. *Elastic annulus under torsional deformation*: demonstrated the ability of the proposed formulation to be used on unstructured grids and reinforced the observation that the standard material point method will converge at the correct rate but only if sufficient material points are used.

5. *Elasto-plastic collapse*: increasing the number of material points per background grid element reduces the magnitude of the stress oscillations, however local stress oscillations still exist. For the generalised interpolation material point method, updating the domains according to the determinant of the deformation gradient causes the domains to exceed the mesh due to insufficient contraction in the vertical direction, whereas updating the domains according to the normal components of the deformation gradient, F_{ii} , results in an over-soft response due to spurious contraction of material point domains due to large rotation components in the deformation gradient.

The numerical examples presented in this paper have highlighted the importance of using sufficient material points per initially populated background element. However, we acknowledge that the use of 9^2+ material points per background grid cell is excessive for routine engineering analysis and we only include these results to demonstrate that errors associated with cell crossing can be mitigated via using a large number of standard material points. A more efficient approach is to adopt a domain-based material point method, such as the generalised interpolation or CPDI2 approaches and use fewer material points per element. The examples have also shown that only the volume-corrected deformation gradient domain update, (38)/(39), and the volume-corrected corner update with mid-side determination, (37), lead to stable results for a range of physical problems that agree well with the more advanced CPDI2 method of Sadeghirad et al. [6]. Although the numerical examples in this paper have focused on two dimensional analysis, the formulations in this paper are general and suitable for three dimensional problems. There have been a number of papers that have analysed three dimensional problems with the material point method (see [7,26,41], amongst others). It is with these problems, where removing the need for remeshing whilst being able to model very large deformations, offers the most promise for the method.

8. Conclusion

Material point methods are unusual in that they are not ideally suited to traditional total and updated Lagrangian formulations of continuum mechanics. This is due to the fact that their basis functions are normally based on material point positions at the start of a load step and assume that calculations take place on the undeformed grid. In the case of updated Lagrangian formulations, this issue can be accounted for by mapping the basis function derivatives into the deformed configuration using the increment in the deformation gradient over the load step [21]. However this introduces an additional computational expense, and algorithm complexity, and the basis function derivatives must be individually mapped for each material point. In this paper we have proposed an alternative material point formulation where the equilibrium equations are satisfied at the nodal positions at the start of the load step. This *previously converged* Lagrangian approach predicts identical results to that of a conventional updated Lagrangian formulation but removes the need to map the derivatives of the basis functions. However, changing the equilibrium frame requires the definition of a new stress measure and also the derivation of an appropriate consistent tangent for large strain elasto-plasticity in order to achieve optimum convergence of the global equilibrium iterations. The new formulation is more computationally efficient than the conventional updated Lagrangian approach for the material point method and can be applied to all existing material point methods available in the literature. However, it should be noted that the primary focus of this paper is on implicit material point methods and the advantages of the proposed formulation are most evident within these methods. Explicit material point methods advance an analysis by forward-predicting from the previous state and for these methods the previously converged formulation reduces to the standard updated Lagrangian method.

This *previously converged* Lagrangian approach has been applied to the standard, generalised interpolation and CPDI2 material point methods and its performance demonstrated on a number of large strain problems with and without analytical solutions. In the case of the generalised interpolation material point method, different domain updating methods have been investigated and a new method proposed which avoids the degenerative properties of existing domain updates which can break down under pure rotation or shearing.

Although the focus of this paper has been on the material point method, the proposed previously converged Lagrangian formulation can also be applied to other numerical methods based on Lagrangian mechanics.

Acknowledgements

This work was supported by the Engineering and Physical Sciences Research Council [grant numbers EP/N006054/1, EP/M017494/1 and EP/M000397/1]. The fifth author (Charlton, T.J.) was supported by the Engineering and Physical Sciences Research Council [grant number EP/K502832/1]. All data created during this research are openly available at <http://doi.org/10.15128/r2pk02c977f>.

Appendix. Consistent tangent moduli

A.1. Updated Lagrangian formulation

The spatial consistent tangent modulus can be expressed as

$$a_{ijkl} = \frac{\partial \sigma_{ij}}{\partial F_{km}} F_{lm} = \frac{1}{2J} D_{ijmn}^{\text{alg}} L_{mnpq} B_{pqkl} - S_{ijkl}, \quad (\text{A.1})$$

where

$$L_{mnpq} = \frac{\partial \ln(b_{mn}^e)}{\partial b_{pq}^e}, \quad B_{pqkl} = \delta_{pk} b_{ql}^e + \delta_{qk} b_{pl}^e, \quad S_{ijkl} = \sigma_{ij} \delta_{jk} \quad (\text{A.2})$$

and D_{ijmn}^{alg} is the small-strain algorithmic tangent obtained from the constitutive model. The derivative of the logarithm of the elastic Cauchy–Green strain tensor with respect to its argument is a special case of the more general formulation given by Miehe [42]. Note that all of the components of a_{ijkl} should be evaluated in the spatial frame — the current deformed configuration.

A.2. Previously converged Lagrangian formulation

The consistent tangent modulus for the previously converged Lagrangian formulation can be expressed as

$$\tilde{a}_{ijkl} = \frac{\partial \tilde{P}_{ij}}{\partial \Delta F_{kl}} = \frac{1}{J_n} \left(\frac{\partial \tau_{im}}{\partial \Delta F_{kl}} (\Delta F^{-1})_{jm} + \tau_{im} \frac{\partial (\Delta F^{-1})_{jm}}{\partial \Delta F_{kl}} \right). \quad (\text{A.3})$$

The derivative of the Kirchhoff stress with respect to the increment in the deformation gradient is

$$\frac{\partial \tau_{ij}}{\partial \Delta F_{kl}} = \frac{1}{2} D_{ijmn}^{\text{alg}} L_{mnpq} \tilde{B}_{pqkl}, \quad (\text{A.4})$$

where

$$\tilde{B}_{ijkl} = \frac{\partial (b_i^e)_{ij}}{\partial \Delta F_{kl}} = \delta_{ik} (b_n^e)_{lb} \Delta F_{jb} + \Delta F_{ia} (b_n^e)_{al} \delta_{jk}, \quad (\text{A.5})$$

the first term in (A.4) is the algorithmic tangent obtained from the small strain constitutive model and L_{ijkl} is given in (A.2). The derivative of the inverse of the increment in the deformation gradient is

$$\frac{\partial (\Delta F^{-1})_{ij}}{\partial \Delta F_{kl}} = -(\Delta F^{-1})_{ik} (\Delta F^{-1})_{lj}. \quad (\text{A.6})$$

References

- [1] D. Sulsky, Z. Chen, H. Schreyer, A particle method for history-dependent materials, *Comput. Methods Appl. Mech. Engrg.* 118 (1994) 179–196.
- [2] J.U. Brackbill, H.M. Ruppel, FLIP - A Method for adaptively zoned, particle-in-cell calculations of fluid flows in two dimensions, *J. Comput. Phys.* 65 (1986) 314–343.

- [3] F. Harlow, The particle-in-cell computing method for fluid dynamics, *Methods Comput. Phys.* 3 (1964).
- [4] S.G. Bardenhagen, E.M. Kober, The generalized interpolation material point method, *Comput. Model. Eng. Sci.* 5 (2004) 477–495.
- [5] A. Sadeghirad, R.M. Brannon, J. Burghardt, A convected particle domain interpolation technique to extend applicability of the material point method for problems involving massive deformations, *Internat. J. Numer. Methods Engng.* 86 (2011) 1435–1456.
- [6] A. Sadeghirad, R. Brannon, J. Guilkey, Second-order convected particle domain interpolation (CPD12) with enrichment for weak discontinuities at material interfaces, *Internat. J. Numer. Methods Engng.* 95 (2013) 928–952.
- [7] V.P. Nguyen, C.T. Nguyen, T. Rabczuk, S. Natarajan, On a family of convected particle domain interpolations in the material point method, *Finite Elements Anal. Des.* 126 (2017) 50–64.
- [8] D.Z. Zhang, X. Ma, P.T. Giguere, Material point method enhanced by modified gradient of shape function, *J. Comput. Phys.* 230 (2011) 6379–6398.
- [9] M. Bü, L.J. Lim, R. Brinkgreve, Application of a second-order implicit material point method, in: *Proceedings of the 1st International Conference on the Material Point Method, MPM 2017*, *Procedia Eng.* 175 (2017) 279–286.
- [10] C. Long, D. Zhang, C. Bronkhorst, G.G. I.I.I., Representing ductile damage with the dual domain material point method, *Comput. Methods Appl. Mech. Engng.* 300 (2016) 611–627.
- [11] T.R. Dhakal, D.Z. Zhang, Material point methods applied to one-dimensional shock waves and dual domain material point method with sub-points, *J. Comput. Phys.* 325 (2016) 301–313.
- [12] M. Gong, Improving the material point method (Ph.D. thesis), The University of New Mexico, Albuquerque, New Mexico, 2015.
- [13] D. Sulsky, M. Gong, Improving the material point method, in: *Innovative Numerical Approaches for Multi-Field and Multi-Scale Problems*, in: *Lecture Notes in Applied and Computational Mechanics*, vol. 81, Springer, 2016, pp. 217–240.
- [14] P.C. Wallstedt, J.E. Guilkey, A weighted least squares particle-in-cell method for solid mechanics, *Internat. J. Numer. Methods Engng.* 85 (2010) 1687–1704.
- [15] Y.G. Motlagh, W.M. Coombs, An implicit high-order material point method, in: *Proceedings of the 1st International Conference on the Material Point Method, MPM 2017*, *Procedia Eng.* 175 (2017) 8–13.
- [16] R. Tielen, E. Wobbes, M. Müller, L. Beuth, A high order material point method, in: *Proceedings of the 1st International Conference on the Material Point Method, MPM 2017*, *Procedia Eng.* 175 (2017) 265–272.
- [17] S. Andersen, L. Andersen, Analysis of spatial interpolation in the material-point method, *Comput. Struct.* 88 (2010) 506–518.
- [18] M. Steffen, P.C. Wallstedt, J.E. Guilkey, R.M. Kirby, M. Berzins, Examination and analysis of implementation choices within the material point method, *Comput. Model. Eng. Sci.* (2008).
- [19] L. Wang, W. Coombs, C. Augarde, M. Cortis, T. Charlton, M. Brown, B.A. Knappett, J.C. Davidson, D. Richards, A. Blake, On the use of domain-based material point methods for problems involving large distortion, *Comput. Methods Appl. Mech. Engng.* (2019) (in press).
- [20] D. Sulsky, H.L. Schreyer, Axisymmetric form of the material point method with applications to upsetting and Taylor impact problems, *Comput. Methods Appl. Mech. Engng.* 139 (1996) 409–429.
- [21] T.J. Charlton, W.M. Coombs, C.E. Augarde, iGIMP: An implicit generalised interpolation material point method for large deformations, *Comput. Struct.* 190 (2017) 108–125.
- [22] L. Moresi, F. Dufour, H.B. Mühlhaus, A Lagrangian integration point finite element method for large deformation modeling of viscoelastic geometries, *J. Comput. Phys.* 184 (2003) 476–497.
- [23] J.E. Guilkey, J.A. Weiss, Implicit time integration for the material point method: Quantitative and algorithmic comparisons with the finite element method, *Internat. J. Numer. Methods Engng.* 57 (2003) 1323–1338.
- [24] S. Cummins, J. Brackbill, An implicit particle-in-cell method for granular materials, *J. Comput. Phys.* 180 (2002) 506–548.
- [25] D. Sulsky, A. Kaul, Implicit dynamics in the material-point method, *Comput. Methods Appl. Mech. Engng.* 193 (2004) 1137–1170.
- [26] W.M. Coombs, T.J. Charlton, M. Cortis, C.E. Augarde, Overcoming volumetric locking in material point methods, *Comput. Methods Appl. Mech. Engng.* 333 (2018) 1–21.
- [27] D. Bigoni, *Nonlinear Solid Mechanics: Bifurcation Theory and Material Instability*, Cambridge University Press, 2012.
- [28] T. Belytschko, W.K. Liu, B. Moran, *Nonlinear Finite Elements for Continua and Structures*, John Wiley & Sons Ltd., 2001.
- [29] Y. Bing, M. Cortis, T.J. Charlton, W.M. Coombs, C.E. Augarde, B-spline based boundary conditions in the material point method, *Comput. Struct.* 212 (2019) 257–274.
- [30] G. Remmerswaal, Development and implementation of moving boundary conditions in the Material Point Method (Master’s thesis), TU Delft, 2017.
- [31] M. Cortis, W.M. Coombs, C.E. Augarde, M.J. Brown, A. Brennan, S. Robinson, Imposition of essential boundary conditions in the material point method, *Internat. J. Numer. Methods Engng.* 113 (2017) 130–152.
- [32] Y. Bing, B-spline based boundary method for the material point method (Master’s thesis), Durham University, 2017.
- [33] T. Molstad, Finite deformation analysis using the finite element method (Ph.D. thesis), University of British Columbia, 1977.
- [34] W.M. Coombs, AMPLE: A material point learning environment, 2019, URL <https://wmcoombs.github.io/>, (Accessed 10 July 2019).
- [35] W.M. Coombs, R.S. Crouch, C.E. Augarde, 70-line 3d finite deformation elastoplastic finite-element code, in: T. Benz, S. Nordal (Eds.), *7th European Conference on Numerical Methods in Geotechnical Engineering, NUMGE, Trondheim, Norway*, pp. 151–156.
- [36] M. Dabrowski, M. Krotkiewski, D.W. Schmid, MILAMIN: MATLAB-based finite element method solver for large problem, *Geochem. Geophys. Geosyst.* 9 (2008).
- [37] R. Bird, W. Coombs, S. Giani, Fast native-MATLAB stiffness assembly for SIPG linear elasticity, *Comput. Math. Appl.* 74 (2017) 3209–3230.
- [38] S. O’Sullivan, R. Bird, W. Coombs, S. Giani, Rapid non-linear finite element analysis of continuous and discontinuous galerkin methods in matlab, *Comput. Math. Appl.* (2019).

- [39] K. Kamojjala, R. Brannon, A. Sadeghirad, J. Guilkey, Verification tests in solid mechanics, *Eng. Comput.* 31 (2015) 193–213.
- [40] B. Wang, P. Vardon, M. Hicks, Investigation of retrogressive and progressive slope failure mechanisms using the material point method, *Comput. Geotech.* 78 (2016) 88–98.
- [41] Y. Lian, P. Yang, X. Zhang, F. Zhang, Y. Liu, P. Huang, A mesh-grading material point method and its parallelization for problems with localized extreme deformation, *Comput. Methods Appl. Mech. Engrg.* 289 (2015) 291–315.
- [42] C. Miehe, Comparison of two algorithms for the computation of fourth-order isotropic tensor functions, *Comput. Struct.* 66 (1998) 37–43.